

Probing the minimal $U(1)_X$ model at future electron-positron colliders via fermion pair-production channels

Arindam Das^{1,2,3,*}, P. S. Bhupal Dev^{4,†}, Yutaka Hosotani^{5,‡} and Sanjoy Mandal^{6,§}

¹Department of Physics, Kyungpook National University, Daegu 41566, Korea

²Institute for the Advancement of Higher Education, Hokkaido University, Sapporo 060-0817, Japan

³Department of Physics, Hokkaido University, Sapporo 060-0810, Japan

⁴Department of Physics and McDonnell Center for the Space Sciences, Washington University, St. Louis, Missouri 63130, USA

⁵Department of Physics, Osaka University, Toyonaka, Osaka 560-0043, Japan

⁶AHEP Group, Institut de Física Corpuscular, CSIC/Universitat de València, Parc Científic de Paterna, C/Catedrático José Beltrán, 2 E-46980 Paterna (Valencia), Spain



(Received 15 December 2021; accepted 6 June 2022; published 21 June 2022)

The minimal $U(1)_X$ extension of the Standard Model (SM) is a well-motivated new physics scenario, where anomaly cancellation dictates new neutral gauge boson (Z') couplings with the SM fermions in terms of the $U(1)_X$ charges of the new scalar fields. We investigate the SM charged fermion pair-production process for different values of these $U(1)_X$ charges at future e^-e^+ colliders: $e^+e^- \rightarrow f\bar{f}$. Apart from the standard γ and Z -mediated processes, this model features additional s -channel (or both s and t -channel when $f = e^-$) Z' exchange which interferes with the SM processes. We first estimate the bounds on the $U(1)_X$ coupling (g') and the Z' mass ($M_{Z'}$) considering the latest dilepton and dijet constraints from the heavy resonance searches at the LHC. Then using the allowed values of g' , we study the angular distributions, forward-backward (\mathcal{A}_{FB}), left-right (\mathcal{A}_{LR}), and left-right forward-backward ($\mathcal{A}_{\text{LR,FB}}$) asymmetries of the $f\bar{f}$ final states. We find that these observables can show substantial deviations from the SM results in the $U(1)_X$ model, thus providing a powerful probe of the multi-TeV Z' bosons at future e^+e^- colliders.

DOI: [10.1103/PhysRevD.105.115030](https://doi.org/10.1103/PhysRevD.105.115030)

I. INTRODUCTION

Although the Standard Model (SM) is on a solid theoretical foundation and has been tested experimentally to great accuracy, it cannot explain the observations of nonzero neutrino masses, dark matter relic density, and matter-antimatter asymmetry in the Universe [1]. These empirical evidences and other theoretical considerations indicate the necessity for an extension of the SM.

A simple beyond the SM (BSM) scenario that can in principle address some of the above-mentioned issues is to extend the SM gauge group by an additional $U(1)$ gauge symmetry. The associated neutral gauge boson (known as

Z') has been extensively studied in the literature due to its wide range of phenomenological aspects; see Refs. [2,3] for reviews. There are many ultraviolet-complete scenarios, where the Z' boson naturally arises, such as in the left-right symmetric models [4–6], and in theories of grand unification based on $SO(10)$ [7,8] and E_6 [9,10]. The Z' bosons also inevitably appear in the gauge-Higgs unification scenario where the Higgs boson is identified with a part of the fifth-dimensional component of the gauge fields, and the Kaluza-Klein (KK) excited modes of the photon and Z boson become Z' bosons [11–16]. Dedicated searches for the Z' boson have been previously carried out at LEP [17] and Tevatron [18,19], but the most stringent bounds on the Z' mass and coupling currently come from the LHC dilepton searches [20,21], which also supersede the low-energy electroweak constraints [22].

In this paper we investigate the future e^+e^- collider prospects of a general but minimal $U(1)_X$ extension of the SM where, in addition to the SM particles, three generations of right-handed neutrinos (RHNs) and a SM-singlet $U(1)_X$ Higgs field are included. The $U(1)_X$ charge assignment for the fermions in this scenario is generation independent which makes the model free from all gauge

*arindamdas@oia.hokudai.ac.jp

†bdev@wustl.edu

‡hosotani@het.phys.sci.osaka-u.ac.jp

§smandal@ific.uv.es

Published by the American Physical Society under the terms of the [Creative Commons Attribution 4.0 International license](https://creativecommons.org/licenses/by/4.0/). Further distribution of this work must maintain attribution to the author(s) and the published article's title, journal citation, and DOI. Funded by SCOAP³.

TABLE I. Particle content of the minimal $U(1)_X$ model where $i(= 1, 2, 3)$ represents the family index. The scalar charges x_H, x_Φ are real parameters. The $B-L$ case is obtained with the choice $x_H = 0$ and $x_\Phi = 1$.

Gauge group	q_L^i	u_R^i	d_R^i	ℓ_L^i	e_R^i	N_R^i	H	Φ
$SU(3)_C$	3	3	3	1	1	1	1	1
$SU(2)_L$	2	1	1	2	1	1	2	1
$U(1)_Y$	1/6	2/3	-1/3	-1/2	-1	0	1/2	0
$U(1)_X$	$\frac{1}{6}x_H + \frac{1}{3}x_\Phi$	$\frac{2}{3}x_H + \frac{1}{3}x_\Phi$	$-\frac{1}{3}x_H + \frac{1}{3}x_\Phi$	$-\frac{1}{2}x_H - x_\Phi$	$-x_H - x_\Phi$	$-x_\Phi$	$-\frac{x_H}{2}$	$2x_\Phi$

and mixed gauge-gravitational anomalies. Reproducing the Yukawa structure of the SM, one finds that the $U(1)_X$ symmetry can be identified as the linear combination of the $U(1)_Y$ in the SM and the $U(1)_{B-L}$ gauge groups [23–26]. Hence the $U(1)_X$ scenario is the generalization of the $U(1)_{B-L}$ extension of the SM [27,28].

Due to the presence of the Z' boson with modest to large couplings to SM fermions under the gauged $U(1)_X$ extension, the model shows a variety of interesting features at the e^+e^- colliders. In particular, the general charge assignment of the particles after the anomaly cancellations leads to potentially large parity violation in the fermion couplings and distinct interference effects in the process $e^-e^+ \rightarrow f\bar{f}$ (where f stands for the SM fermions). We investigate this process for both leptonic and hadronic final states, by analyzing the cross sections as well as different kinematic observables, including the forward-backward asymmetry (\mathcal{A}_{FB}), left-right asymmetry (\mathcal{A}_{LR}), and left-right forward-backward asymmetry ($\mathcal{A}_{LR,FB}$). We show that even if the Z' boson is sufficiently heavy and off-shell (even inaccessible at the LHC), large deviations from the SM expectations in the angular distributions, forward-backward asymmetries, left-right asymmetries, and left-right forward-backward asymmetries can be seen at the proposed e^-e^+ colliders.¹ We consider various center-of-mass energy values $\sqrt{s} = 250$ GeV, 500 GeV, 1 TeV, and 3 TeV to illustrate this effect. Furthermore, we take special care for the $e^-e^+ \rightarrow e^-e^+$ Bhabha process, which can proceed via either s or t -channel Z' boson, in addition to the SM γ and Z exchanges. Here we study the deviations in differential and total cross sections, and in left-right asymmetry from the SM results, which are then compared with the theoretically estimated statistical errors.

It is worth noting here that to obtain the bounds on the Z' boson at the LHC, the CMS and ATLAS Collaborations use the so-called sequential SM where the couplings of the Z' boson with the fermions are exactly the same as those of the SM Z boson [30]. In our $U(1)_X$ scenario, we reinterpret these bounds, properly taking into account the appropriate Z' branching ratios to dileptons, and obtain the updated

¹Similar consequences have been predicted in the $SO(5) \times U(1) \times SU(3)$ gauge-Higgs unification formulated in the Randall-Sundrum warped space in which the KK modes of the photon, Z boson, and Z_R boson play the role of Z' bosons [29].

limits on the $U(1)_X$ gauge coupling (g') as a function of the Z' mass, which are then used in our numerical analysis for $e^+e^- \rightarrow f\bar{f}$.

The paper is organized as follows. We discuss the $U(1)_X$ model, model parameters, and the constraints on the g' in Sec. II. We study different observables related to the $e^-e^+ \rightarrow f\bar{f}$ scattering process for $f \neq e$ in Sec. III. We discuss the Bhabha scattering in Sec. IV. Some discussion on usefulness of the kinematic variables is given in Sec. V. We finally conclude the paper in Sec. VI.

II. THE $U(1)_X$ MODEL

The model we consider here is based on the gauge group $SU(3)_C \otimes SU(2)_L \otimes U(1)_Y \otimes U(1)_X$. The particle content is shown in Table I. In addition to the SM particles, three generations of the RHNs are introduced to cancel the gauge and mixed gauge-gravity anomalies. There also exists a SM-singlet scalar Φ which generates the Majorana mass term for the RHNs after the $U(1)_X$ symmetry breaking. The RHNs couples to the SM lepton (ℓ_L) and Higgs (H) doublets to generate the Dirac Yukawa couplings that go into the seesaw mechanism for neutrino masses [31–35]. To introduce the fermion mass terms and the flavor mixings, the Yukawa interaction can be written as

$$\begin{aligned} \mathcal{L}^{\text{Yukawa}} = & -Y_u^{\alpha\beta} \bar{q}_L^\alpha H u_R^\beta - Y_d^{\alpha\beta} \bar{q}_L^\alpha \tilde{H} d_R^\beta - Y_e^{\alpha\beta} \bar{\ell}_L^\alpha \tilde{H} e_R^\beta \\ & - Y_\nu^{\alpha\beta} \bar{\ell}_L^\alpha H N_R^\beta - Y_N^\alpha \Phi \bar{N}_R^{\alpha c} N_R^\alpha + \text{H.c.}, \end{aligned} \quad (1)$$

where $\tilde{H} \equiv i\tau^2 H^*$ (τ^2 being the second Pauli matrix). The $U(1)_X$ charges of all the particles are shown in Table I after solving the gauge and mixed gauge-gravity anomalies [25] and using the Yukawa interaction from Eq. (1). We see that $x_H = 0$ and $x_\Phi = 1$ will reproduce the $B-L$ scenario. From the structure of the individual charges we can confer that the $U(1)_X$ gauge group can be considered as a linear combination of the $U(1)_Y$ and $U(1)_{B-L}$ gauge groups. The $U(1)_X$ gauge coupling g' is a free parameter of our model which appears as either $g'x_H$ or $g'x_\Phi$ in the interaction Lagrangian. Without the loss of generality we fix $x_\Phi = 1$ in this paper. As a result x_H acts as an angle between the $U(1)_Y$ and $U(1)_{B-L}$ directions. In the limits $x_H \rightarrow -\infty$ ($+\infty$), $U(1)_X$ is (anti-)aligned to the $U(1)_Y$ direction.

The renormalizable Higgs potential of the model is given by

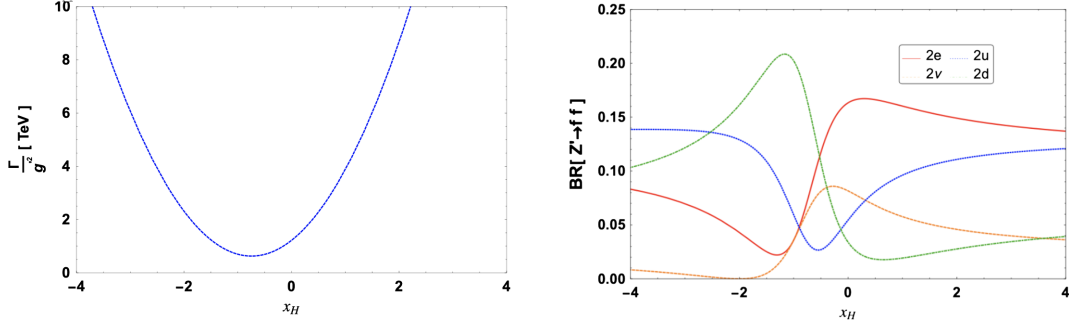


FIG. 1. Total decay width of Z' (left panel) and its branching ratios into single-generation fermions (right panel) as a function of x_H for $M_{Z'} = 7.5$ TeV and $x_\Phi = 1$. We normalize the total decay width by g^2 .

$$V = -m_h^2(H^\dagger H) + \lambda(H^\dagger H)^2 + m_\Phi^2(\Phi^\dagger \Phi) + \lambda_\Phi(\Phi^\dagger \Phi)^2 + \lambda'(H^\dagger H)(\Phi^\dagger \Phi). \quad (2)$$

In the limit of small λ' , the mixing between the scalar fields H and Φ is negligible, so they can be analyzed separately [25,36]. After the electroweak and $U(1)_X$ symmetry breaking the scalar fields H and Φ develop their vacuum expectation values (VEVs)

$$\langle H \rangle = \frac{1}{\sqrt{2}} \begin{pmatrix} v+h \\ 0 \end{pmatrix}, \quad \text{and} \quad \langle \Phi \rangle = \frac{v_\Phi + \phi}{\sqrt{2}}. \quad (3)$$

At the potential minimum where the electroweak scale is marked with $v \simeq 246$ GeV, v_Φ is considered to be a free parameter with $v_\Phi^2 \gg v^2$. After the symmetry breaking, the mass of the $U(1)_X$ gauge boson (Z') can be expressed as

$$M_{Z'} = g' \sqrt{4v_\Phi^2 + \frac{1}{4}x_H^2 v^2} \simeq 2g'v_\Phi. \quad (4)$$

The $U(1)_X$ VEV governs the Majorana mass term for the RHNs from the fifth term of Eq. (1) and the electroweak VEV generates the Dirac neutrino mass term from the fourth term of Eq. (1). They can be written as $m_{N_\alpha} = \frac{Y_N^\alpha}{\sqrt{2}} v_\Phi$ and $m_D^{\alpha\beta} = \frac{Y_v^{\alpha\beta}}{\sqrt{2}} v$, respectively. Hence the full neutrino mass mixing can be written as

$$\mathcal{M}_\nu = \begin{pmatrix} 0 & m_D \\ m_D^T & m_N \end{pmatrix}. \quad (5)$$

Diagonalizing Eq. (5) the light neutrino mass can be generated as $m_\nu \simeq -m_D m_N^{-1} m_D^T$ in the seesaw limit [31–35].

A. Z' interactions with fermions

Due to the presence of the general $U(1)_X$ charges ($q_x^{L,R}$) shown in Table I, the Z' interactions with the SM quarks (q) and leptons (ℓ) can be written as

$$\mathcal{L}^q = -g'(\bar{q}\gamma^\mu q_x^{qL} P_L q + \bar{q}\gamma^\mu q_x^{qR} P_R q)Z'_\mu - g'(\bar{\ell}\gamma^\mu \ell_x^{\ell L} P_L \ell + \bar{\ell}\gamma^\mu \ell_x^{\ell R} P_R \ell)Z'_\mu, \quad (6)$$

where P_L and P_R are the left and right projection operators $(1 \mp \gamma_5)/2$, respectively. Using Eq. (6) we can calculate the partial decay widths of Z' into the SM fermions. For charged fermions, we get

$$\Gamma(Z' \rightarrow f\bar{f}) = N_c \frac{M_{Z'}}{24\pi} (g_L^f [g', x_H, x_\Phi]^2 + g_R^f [g', x_H, x_\Phi]^2), \quad (7)$$

where $N_c = 3(1)$ is a color factor for the quarks (leptons) and $g_{L(R)}^f [g', x_H, x_\Phi]$ is the coupling of the Z' with left-(right-) handed charged fermions, which depends on the $U(1)_X$ charges. The partial decay width of the Z' into a pair of single-generation light neutrinos can be written as

$$\Gamma(Z' \rightarrow \nu\bar{\nu}) = \frac{M_{Z'}}{24\pi} g_L^{\nu} [g', x_H, x_\Phi]^2. \quad (8)$$

The partial decay width of the Z' into a pair of RHNs can be written as

$$\Gamma(Z' \rightarrow NN) = \frac{M_{Z'}}{24\pi} g_R^N [g', x_\Phi]^2 \left(1 - 4 \frac{m_N^2}{M_{Z'}^2}\right)^{\frac{3}{2}}. \quad (9)$$

However, in this analysis we assume for simplicity that the decay of the Z' into a pair of RHNs is kinematically disallowed because $m_N > M_{Z'}$.²

Using the partial decay widths of Z' from Eqs. (7) and (8) we show the variation in total decay width of the Z' (Γ), normalized by g^2 , as a function of x_H in the left panel of Fig. 1 for $M_{Z'} = 7.5$ TeV and $x_\Phi = 1$. The branching ratios of Z' into single-generation SM fermions are shown in the right panel of Fig. 1 as a function of x_H . It is clear that the Z' total decay width and branching ratios depend on the x_H

²For the collider phenomenology of TeV scale RHNs in the general $U(1)_X$ model, see, e.g., Refs. [37–41].

TABLE II. The $U(1)_X$ charges of the particles for different values of x_H taking $x_\Phi = 1$. Here $i = 1, 2, 3$ represents the generation index. $x_H = -2$ and 0 are the $U(1)_R$ and $B - L$ cases, respectively. The SM charges are shown in Table I.

$U(1)_X$	q_L^i	u_R^i	d_R^i	ℓ_L^i	e_R^i	N_R^i	H	Φ
x_H	$\frac{1}{6}x_H + \frac{1}{3}x_\Phi$	$\frac{2}{3}x_H + \frac{1}{3}x_\Phi$	$-\frac{1}{3}x_H + \frac{1}{3}x_\Phi$	$-\frac{1}{2}x_H - x_\Phi$	$-x_H - x_\Phi$	$-x_\Phi$	$-\frac{x_H}{2}$	$2x_\Phi$
-2	0	-1	1	0	1	-1	1	2
-1	$\frac{1}{6}$	$-\frac{1}{3}$	$\frac{2}{3}$	$-\frac{1}{2}$	0	-1	$\frac{1}{2}$	2
$-\frac{1}{2}$	$\frac{1}{4}$	0	$\frac{1}{2}$	$-\frac{3}{4}$	$-\frac{1}{2}$	-1	$\frac{1}{4}$	2
0	$\frac{1}{3}$	$\frac{1}{3}$	$\frac{1}{3}$	-1	-1	-1	0	2
$\frac{1}{2}$	$\frac{5}{12}$	$\frac{1}{2}$	$\frac{1}{6}$	$-\frac{5}{4}$	$-\frac{3}{2}$	-1	$\frac{1}{4}$	2
1	$\frac{1}{2}$	1	0	$-\frac{3}{2}$	-2	-1	$\frac{1}{4}$	2
2	$\frac{1}{3}$	$\frac{5}{3}$	$-\frac{1}{3}$	-2	-3	-1	1	2

charge. In particular, the total decay width is minimum at $x_H = -0.8$. Also, the leptonic (or hadronic) branching ratios can be suppressed for a suitable choice of x_H , thereby relaxing the LHC dilepton (or dijet) bounds on Z' , as discussed below.

B. Collider bounds

The $U(1)_X$ charges of the particles for different values of x_H with $x_\Phi = 1$ are given in Table II. We will use these benchmark x_H values in our following analysis. For $x_H = -2$ there is no interaction of Z' with left-handed quarks or leptons. For $x_H = -1$ there is no interaction between right-handed charged leptons and Z' . Similarly, the right-handed up- (down)-type quarks have no interaction with Z' for $x_H = -0.5(1)$.

First we evaluate the LEP constraints on the model parameters for different values of x_H considering $M_{Z'} \gg \sqrt{s}$. Following Refs. [17,42,43] we parametrize the contact interactions for the process $e^+e^- \rightarrow f\bar{f}$ by an effective Lagrangian

$$\mathcal{L}_{\text{eff}} = \frac{g^2}{(1 + \delta_{ef})(\Lambda_{AB}^{f\pm})^2} \sum_{A,B=L,R} \eta_{AB} (\bar{e}\gamma^\mu P_A e) (\bar{f}\gamma_\mu P_B f), \quad (10)$$

where $g^2/4\pi$ is taken to be 1 by convention, $\delta_{ef} = 1(0)$ for $f = e$ ($f \neq e$), $\eta_{AB} = \pm 1$ or 0 , and $\Lambda_{AB}^{f\pm}$ is the scale of the contact interaction, having either constructive (+) or destructive (-) interference with the SM processes $e^+e^- \rightarrow f\bar{f}$ [44]. Following Ref. [45] we calculate the Z' exchange matrix element for our process as

$$\frac{g^2}{M_{Z'}^2 - s} [\bar{e}\gamma^\mu (x'_\ell P_L + x'_e P_R) e] [\bar{f}\gamma_\mu (x_{f_L} P_L + x_{f_R} P_R) f], \quad (11)$$

where x'_ℓ and x'_e are the $U(1)_X$ charges of e_L and e_R , respectively, and similarly, x_{f_L} and x_{f_R} are the $U(1)_X$

charges of f_L and f_R , respectively, all of which can be found in Table II. Matching Eqs. (10) and (11) we evaluate the following bound on $M_{Z'}$ as

$$M_{Z'}^2 \gtrsim \frac{g^2}{4\pi} |x_{e_A} x_{f_B}| (\Lambda_{AB}^{f\pm})^2, \quad (12)$$

considering $M_{Z'}^2 \gg s$ where $\sqrt{s} = 209$ GeV for LEP-II. Using Eq. (12), we can translate the LEP bounds on $\Lambda_{AB}^{f\pm}$ reported in Ref. [17] to the bounds on $M_{Z'}/g'$ as a function of x_H , as shown in Fig. 2 by the gray-shaded region. We use the 95% confidence level (C.L.) limits on Λ^\pm from Ref. [17] for both hadronic and leptonic channels, where for the latter, we assume universality in the contact interactions. Moreover, for any given x_H value, we consider all possible chirality structures, i.e., $AB = LL, RR, LR, RL, VV$, and AA . The exclusion contour shown in Fig. 2 is obtained by taking the boundary of the most stringent bounds. Using the same procedure, we also estimate the prospective reaches at the ILC with $\sqrt{s} = 250$ GeV, 500 GeV, and 1 TeV from the $\Lambda_{AB}^{f\pm}$ values reported in Ref. [46], as represented by red dotted,

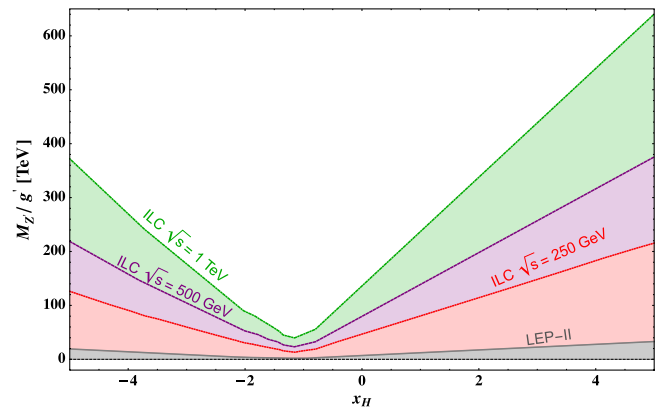


FIG. 2. Current LEP bound on $M_{Z'}/g'$ for different x_H values (gray shaded) and the future ILC projections for $\sqrt{s} = 250$ GeV (red shaded), 500 GeV (purple shaded), and 1 TeV (green shaded).

TABLE III. The 95% C.L. lower limits on $M_{Z'}/g'$ in the $U(1)_X$ model from $e^+e^- \rightarrow f\bar{f}$ processes in the contact interaction limit for different values of x_H . These results are obtained by recasting the limits on the scale Λ^\pm quoted in Refs. [17,46] and taking the most stringent limit out of all the different channels considered there.

Machine	\sqrt{s}	95% C.L. lower limit on $M_{Z'}/g'$ (in TeV)						
		$x_H = -2$	$x_H = -1$	$x_H = -0.5$	$x_H = 0$	$x_H = 0.5$	$x_H = 1$	$x_H = 2$
LEP-II	209 GeV	5.0	2.2	4.4	7.0	10.3	11.1	18.0
ILC	250 GeV	31.6	16.3	29.5	48.2	64.3	79.0	113.7
	500 GeV	54.4	26.3	50.1	81.6	110.2	139.1	199.7
	1 TeV	88.6	47.7	84.8	137.2	185.8	238.2	339.2

purple dashed, and green dot-dashed lines, respectively, in Fig. 2. Our results are summarized in Table III for some benchmark values of x_H to be used in our subsequent analysis.

We can easily translate the limits on $\frac{M_{Z'}}{g'}$ from Fig. 2 for different x_H values onto the $M_{Z'} - g'$ plane, as shown in Fig. 3 for fixed values of $x_H = -2, -1, -0.5, 0, 0.5, 1, 2$. The LEP exclusion is again shown by the gray-shaded region, while the future ILC prospects are shown by the unshaded magenta dot-dashed, dashed, and dotted lines for $\sqrt{s} = 250$ GeV, 500 GeV, and 1 TeV, respectively.

For comparison, we also calculate the hadron collider bounds in the $M_{Z'} - g'$ plane for different x_H values by recasting the current ATLAS and CMS search results for Z' in both dilepton [20,21] and dijet [47,48] channels, as shown in Fig. 3 by various shaded regions. In each case, we calculate the Z' -mediated production cross section in our model (σ_{Model}) for a given $M_{Z'}$ with fixed x_H , properly taking into account the modified branching ratios, and compare it to the observed 95% C.L. limit on the cross section (σ_{Obs}) to derive an upper bound on the coupling strength

$$g' = \sqrt{g_{\text{Model}}^2 \left(\frac{\sigma_{\text{Obs}}}{\sigma_{\text{Model}}} \right)}, \quad (13)$$

where g'_{Model} is the coupling considered to calculate σ_{Model} . The FeynRules file of the model can be found in [50]. For the dilepton channel, we consider the electrons and muons combined to derive the limits shown in Fig. 3. We also consider the future high-luminosity phase of the LHC (HL-LHC) at $\sqrt{s} = 14$ TeV with 3 ab^{-1} integrated luminosity and draw the projected dilepton bounds following the analysis given in the ATLAS technical design report (TDR) [49].

From Fig. 3, we find that the LHC dilepton constraints are the most stringent up to $M_{Z'} = 6$ TeV, beyond which the resonant Z' production is kinematically limited at $\sqrt{s} = 13$ TeV LHC. For the same kinematic reason, the mass reach is not expected to improve much with the $\sqrt{s} = 14$ TeV data, as indicated in Fig. 3 by the green dotted curve. On the other hand, lepton colliders provide better

sensitivity for heavy Z' bosons, going well beyond the LHC reach. As we will show in the subsequent sections, future lepton colliders are not only sensitive to $M_{Z'} \gg \sqrt{s}$, but also provide crucial post-discovery characterization of Z' via different asymmetry observables. In particular, due to the different couplings of the Z' to left- and right-handed SM fermions for different x_H values, these asymmetries can help us easily distinguish the $U(1)_X$ Z' from the $B - L$ Z' which has the same couplings to the left- and right-handed fermions.

To illustrate our point, for the rest of this paper we will consider a specific benchmark value of $M_{Z'} = 7.5$ TeV, which is just beyond the LHC reach. From Fig. 3, we find that the strongest limits on g' for $M_{Z'} = 7.5$ TeV comes from LEP-II, which are 0.9, 0.9, 0.6, and 0.4 for $x_H = -2, -1, 1, 2$, respectively. In view of this, we will consider a common benchmark value of $g' = 0.4$ for $x_H = -2, -1, 1, 2$ to study the kinematic observables at future e^-e^+ colliders. It is straightforward to extend our analysis for other choices of $M_{Z'}$, g' , or x_H values.

In Table III, we have used ILC with different \sqrt{s} options just as a representative for future e^+e^- machines. Our analysis in this work is equally valid for other e^+e^- collider proposals. For completeness, we summarize in Fig. 4 the expected run time, total integrated luminosity, and the center-of-mass energy options for four future e^+e^- collider proposals currently being discussed, namely, FCC-ee [51], CEPC [52], ILC [53], and CLIC [54]. In the following, we will generically consider the possibilities of $\sqrt{s} = 250$ GeV, 500 GeV, 1 TeV, and 3 TeV, all with $\mathcal{L}_{\text{int}} = 1 \text{ ab}^{-1}$.

III. KINEMATIC OBSERVABLES FOR THE $e^-e^+ \rightarrow f\bar{f}$ ($f \neq e$) PROCESS

First we discuss the case of $f \neq e$ in the process $e^-e^+ \rightarrow f\bar{f}$, which only gets s -channel contributions from neutral gauge bosons, i.e., γ and Z for the SM, and γ , Z , and Z' for the $U(1)_X$ model. The additional contributions in the $U(1)_X$ case will be observed from the interfere of Z' with the γ and Z -mediated processes. In this model, quarks and leptons are differently charged under $U(1)_X$ (cf. Table II) which can be manifested in their interactions with Z' . Similarly, the left- and right-handed fermions are differently charged under $U(1)_X$ which affects their interactions

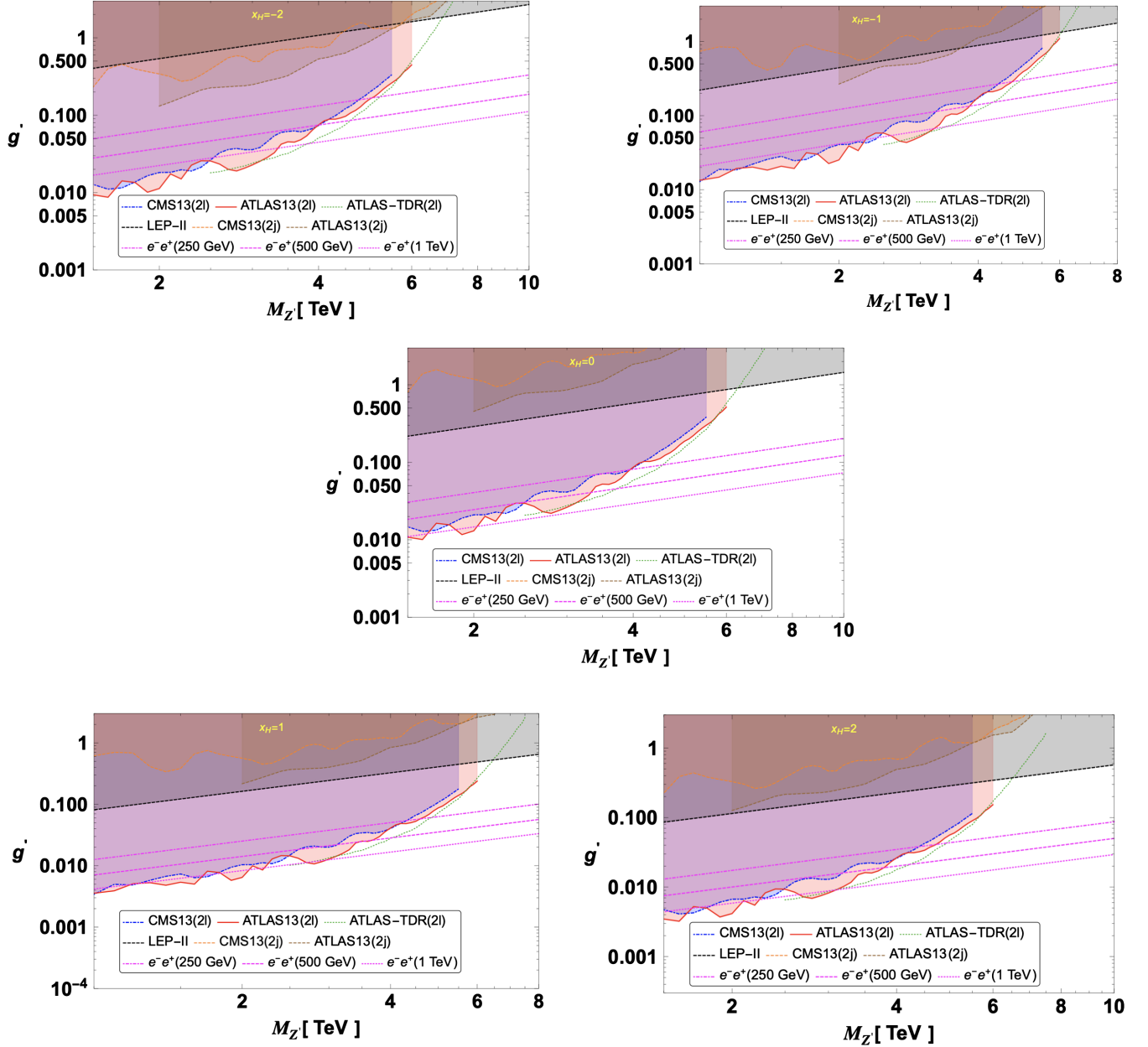
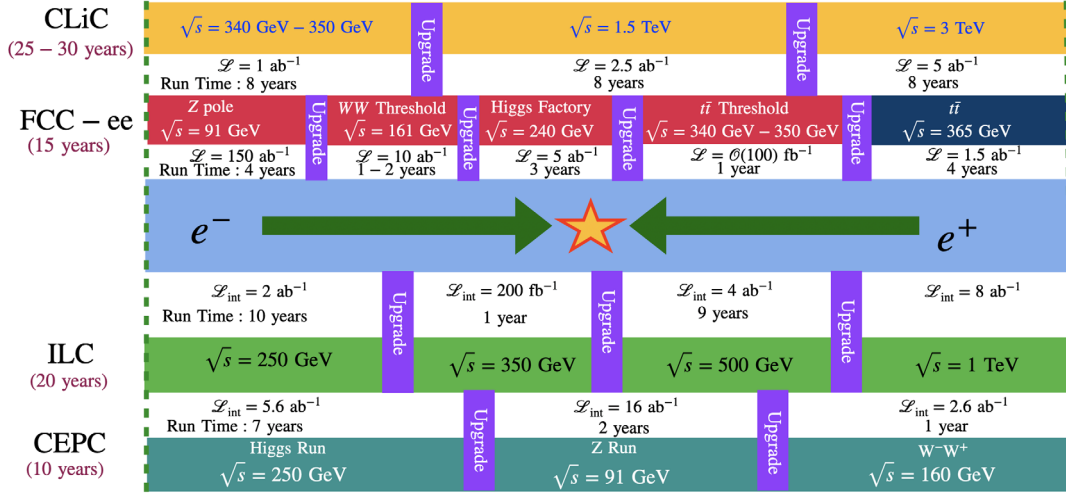


FIG. 3. Limits on g' as a function of $M_{Z'}$ for different x_H values and with $x_\Phi = 1$. The shaded regions are ruled out by the current experimental data from LEP-II [17], and LHC dilepton [20,21], and dijet [47,48] searches. The future HL-LHC [49], as well as the ILC prospects (this work), are also shown as unshaded curves for comparison. The middle panel with $x_H = 0$ is the $B - L$ case.

with Z' . Since the $U(1)_X$ charge and gauge coupling are assumed to be family universal, we will consider the representative case of $f = \mu$ for leptonic final states, and $f = b$ and t , respectively, for the down-type and up-type quark final states in the process $e^-e^+ \rightarrow f\bar{f}$. Note that in a realistic detector environment, the top quarks can only be identified by their decay products, i.e., bottom quarks and W bosons (which are further characterized depending on whether they decay leptonically or hadronically). However, for simplicity, we restrict our study of the Z' effect in the $e^-e^+ \rightarrow f\bar{f}$ process to parton level only, which already

illustrates the main points we want to emphasize, and moreover, all the numerical results presented here can be understood analytically. A full detector-level simulation, including systematic effects, detector efficiency for the leptons, and misidentification of jets or leptons, is beyond the scope of the current work, and will be pursued elsewhere. Such a detailed study will be more relevant when the actual e^+e^- collider is built.

We capture the Z' effects in the process $e^-e^+ \rightarrow f\bar{f}$ by considering several kinematic observables, as described below.


 FIG. 4. The run time, \sqrt{s} , and \mathcal{L}_{int} for different proposed e^-e^+ colliders.

A. Differential cross section

Let us first consider the differential scattering cross sections for the processes $e^-_L e^+_R \rightarrow f\bar{f}$ and $e^-_R e^+_L \rightarrow f\bar{f}$, which can be, respectively, written as

$$\begin{aligned} \frac{d\sigma^{\text{LR}}}{d\cos\theta} &= \frac{\beta s}{32\pi} \left[(1 + \beta^2 \cos^2\theta) (|q^{e_L f_L}|^2 + |q^{e_L f_R}|^2) \right. \\ &\quad + 2\beta \cos\theta (|q^{e_L f_L}|^2 - |q^{e_L f_R}|^2) \\ &\quad \left. + 8 \frac{m_f^2}{s} \{\text{Re}(q^{e_L f_L} q^{e_L f_R*})\} \right], \end{aligned} \quad (14)$$

$$\begin{aligned} \frac{d\sigma^{\text{RL}}}{d\cos\theta} &= \frac{\beta s}{32\pi} \left[(1 + \beta^2 \cos^2\theta) (|q^{e_R f_R}|^2 + |q^{e_R f_L}|^2) \right. \\ &\quad + 2\beta \cos\theta (|q^{e_R f_R}|^2 - |q^{e_R f_L}|^2) \\ &\quad \left. + 8 \frac{m_f^2}{s} \{\text{Re}(q^{e_R f_L} q^{e_R f_R*})\} \right], \end{aligned} \quad (15)$$

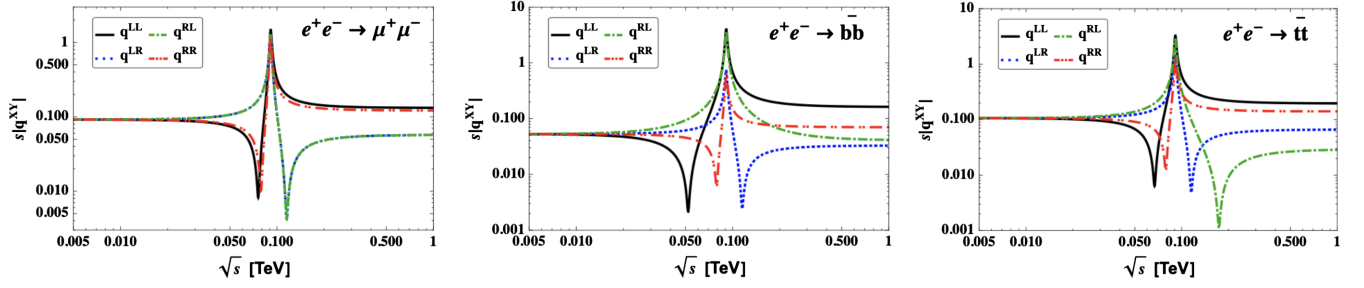
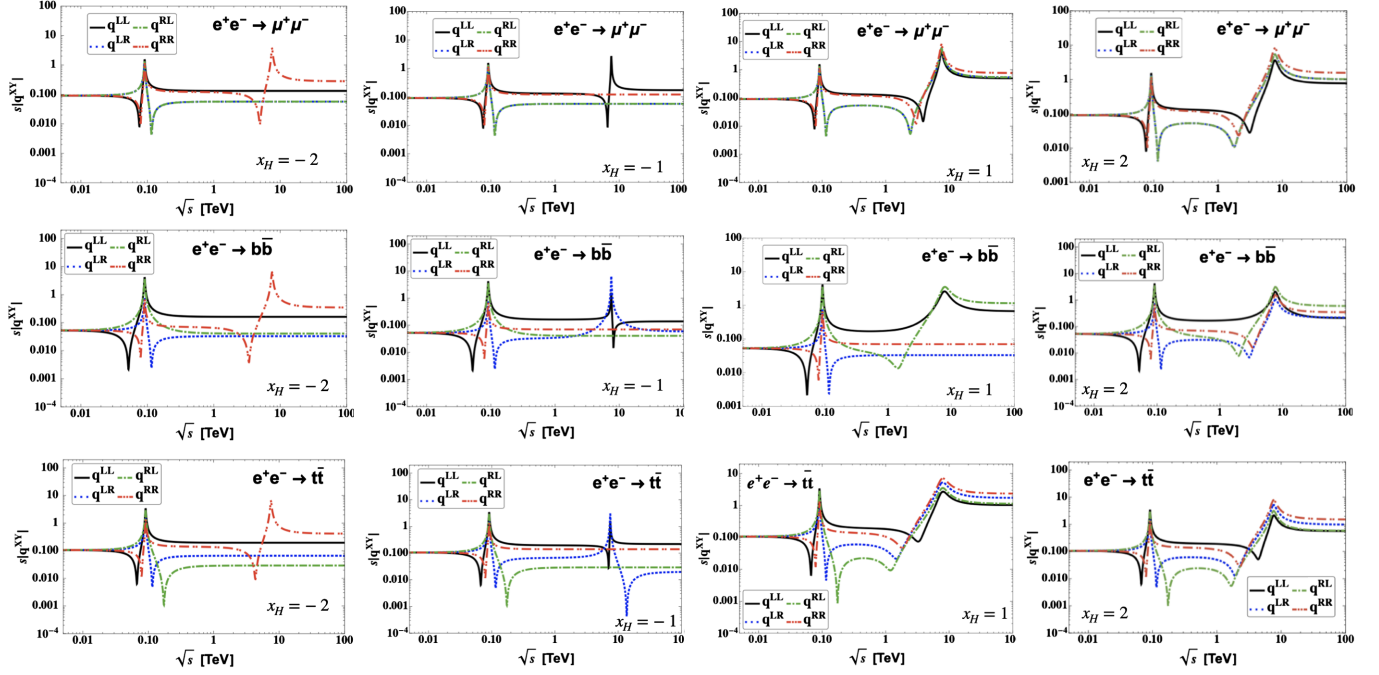
where θ is the scattering angle, m_f is the final state fermion mass and $\beta = \sqrt{1 - \frac{4m_f^2}{s}}$. In the high energy collider limit when $m_f \ll \sqrt{s}$, we obtain $\beta \rightarrow 1$. In Eqs. (14) and (15) we use the quantities $q^{e_L f_L}$, $q^{e_L f_R}$, $q^{e_R f_L}$, and $q^{e_R f_R}$ which can be defined as

$$\begin{aligned} q^{e_L f_L} &= \sum_i \frac{g_L^{V_i e} g_L^{V_i f}}{s - m_{V_i}^2 + im_{V_i} \Gamma_{V_i}}, \\ q^{e_L f_R} &= \sum_i \frac{g_L^{V_i e} g_R^{V_i f}}{s - m_{V_i}^2 + im_{V_i} \Gamma_{V_i}}, \\ q^{e_R f_L} &= \sum_i \frac{g_R^{V_i e} g_L^{V_i f}}{s - m_{V_i}^2 + im_{V_i} \Gamma_{V_i}}, \\ q^{e_R f_R} &= \sum_i \frac{g_R^{V_i e} g_R^{V_i f}}{s - m_{V_i}^2 + im_{V_i} \Gamma_{V_i}}, \end{aligned} \quad (16)$$

where $g_{L(R)}^{V_i e/f}$ are the coupling of the left- (right-) handed electron/fermion to the vector boson $V_i = \gamma, Z, Z'$, with m_{V_i} and Γ_{V_i} being the corresponding vector boson mass and total decay width.

From Eq. (16) we define a quantity $s|q^{XY}|$, where the indices X and Y indicate the handedness of the initial state electron and final state fermion, respectively. In other words, we choose quantities like $s|q^{LL}|$, $s|q^{LR}|$, $s|q^{RL}|$, and $s|q^{RR}|$ in accordance with Eq. (16), which reflect the nature of the SM and BSM propagators. We first present the quantities $s|q^{XY}|$ as a function of \sqrt{s} for the SM case in Fig. 5, taking $f = \mu, b$, and t from left to right, respectively. One can clearly see the Z resonance at $\sqrt{s} = M_Z$ in all the cases. The additional dips are caused by the destructive interference between the γ and Z -mediated processes, and the exact locations of these dips depend on the chirality structure of the initial and final state fermions (and also on the top quark mass in the $t\bar{t}$ case).

Now we include the Z' contribution in Eq. (16) and show the effect on $s|q^{XY}|$ in Fig. 6 for $M_{Z'} = 7.5$ TeV and for $x_H = -2, -1, 1$, and 2 , respectively, from the left to right panels. The three rows are for $f\bar{f} = \mu^+\mu^-$ (top), $b\bar{b}$ (middle), and $t\bar{t}$ (bottom). The SM and BSM propagators are the same except for the presence of Z' in the BSM case. As a result, a broad resonance now occurs at $\sqrt{s} = M_{Z'}$. Here we have taken a relatively large $g' = 0.4$ for $M_{Z'} = 7.5$ TeV, which helps to produce this broad resonance. An increase in \sqrt{s} will not show further resonance peaks for the SM case; therefore we restrict the SM case up to 1 TeV only in Fig. 5. However, in the $U(1)_X$ case, we show up to $\sqrt{s} = 100$ TeV in Fig. 6. We notice that the quantity $s|q^{XY}|$ becomes independent of \sqrt{s} when $\sqrt{s} \gg M_{Z'}$ and leading to almost flat curves mimicking the nature of an effective theory for large s . It happens due to the fact that both $\frac{m_{V_i}^2}{s} \ll 1$ and $\frac{m_{V_i} \Gamma_{V_i}}{s} \ll 1$ in this limit.

FIG. 5. $s|q^{XY}|$ as a function of \sqrt{s} in the SM for the $e^-e^+ \rightarrow f\bar{f}$ process.FIG. 6. $s|q^{XY}|$ as a function of \sqrt{s} in the $U(1)_X$ model for the $e^-e^+ \rightarrow f\bar{f}$ process considering $M_{Z'} = 7.5$ TeV, $g' = 0.4$.

From Table II and Eq. (16) it is evident that for $x_H = -2$ the couplings of Z' with q_L and e_L are zero. Therefore only the quantity $s|q^{RR}|$ gives a resonance at $M_{Z'}$, as shown in the left column of Fig. 6. For $x_H = -1$, there is no coupling between e_R and Z' ; as a result only $s|q^{LL}|$ contributes to the Z' resonance in the $e^-e^+ \rightarrow \mu^+\mu^-$ process, as shown in the top row, second column, whereas both $s|q^{LL}|$ and $s|q^{RL}|$ contribute in the $b\bar{b}$ and $t\bar{t}$ cases. In the case of $x_H = 1$ the coupling between d_R and Z' vanishes; therefore, the Z' contributions from $s|q^{LL}|$ and $s|q^{RL}|$ only are observed in the $e^-e^+ \rightarrow b\bar{b}$ process. At $x_H = 2$ all the charged fermions have nonvanishing couplings with Z' .³ The effects of Z' on the q^{XY} observables depending on the x_H values are summarized in Table IV.

³For completeness we point out that at $x_H = -0.5$, the coupling between u_R and Z' is zero. This scenario can be observed for the process $e^-e^+ \rightarrow t\bar{t}$, where the quantities $s|q^{LL}|$ and $s|q^{RL}|$ only contribute to the Z' resonance.

B. Total cross section

An important advantage of lepton colliders is that the incoming beams can be polarized. Let us consider the polarized electron and positron beams with the polarization fractions P_{e^-} and P_{e^+} , respectively. The differential scattering cross section of the process $e^-e^+ \rightarrow f\bar{f}$ can be written as

TABLE IV. Effect of the Z' -induced interactions on q^{XY} defined in Eq. (16) due to different values of x_H in the $e^-e^+ \rightarrow f\bar{f}$ process.

x_H	Interaction	Z' contribution observable for
-2	No interaction between f_L and Z'	q^{eRfR} in $e^-e^+ \rightarrow \mu^+\mu^-$, $b\bar{b}$, $t\bar{t}$
-1	No interaction between e_R and Z'	q^{eLfL} in $e^-e^+ \rightarrow \mu^+\mu^-$ q^{eLfL}, q^{eLfR} in $e^-e^+ \rightarrow b\bar{b}, t\bar{t}$
1	No interaction between d_R and Z'	q^{eLfL}, q^{eRfL} in $e^-e^+ \rightarrow b\bar{b}$ All q^{XY} in $\mu^+\mu^-$ and $t\bar{t}$
2	All interactions hold	All q^{XY} in $e^-e^+ \rightarrow f\bar{f}$

$$\begin{aligned} \frac{d\sigma}{d\cos\theta}(P_{e^-}, P_{e^+}, \cos\theta) &= \frac{\sigma^{U(1)_X}}{\sigma_{\text{SM}}}(P_{e^-}, P_{e^+}) - 1, \quad (23) \\ &= (1 - P_{e^-}P_{e^+})\frac{1}{4}\left\{(1 - P_{\text{eff}})\frac{d\sigma^{\text{LR}}(\cos\theta)}{d\cos\theta}\right. \\ &\quad \left.+ (1 + P_{\text{eff}})\frac{d\sigma^{\text{RL}}(\cos\theta)}{d\cos\theta}\right\}, \quad (17) \end{aligned}$$

where $P_{\text{eff}} = \frac{P_{e^-} - P_{e^+}}{1 - P_{e^-}P_{e^+}}$ is the effective polarization, and the differential cross sections $\frac{d\sigma^{\text{LR}}}{d\cos\theta}$ and $\frac{d\sigma^{\text{RL}}}{d\cos\theta}$ have been defined in Eqs. (14) and (15), respectively. From Eq. (17) we calculate the total cross section by integrating over the scattering angle as

$$\sigma(P_{e^-}, P_{e^+}) = \int_{-\cos\theta_{\text{max}}}^{\cos\theta_{\text{max}}} d\cos\theta \frac{d\sigma}{d\cos\theta}(P_{e^-}, P_{e^+}, \cos\theta), \quad (18)$$

where θ_{max} depends upon the experiment. Theoretically using $\cos\theta_{\text{max}} = 1$ we get

$$\begin{aligned} \sigma(P_{e^-}, P_{e^+}) &= (1 - P_{e^-}P_{e^+})\frac{1}{4}[(1 - P_{\text{eff}})\sigma^{\text{LR}} \\ &\quad + (1 + P_{\text{eff}})\sigma^{\text{RL}}], \quad (19) \end{aligned}$$

$$\begin{aligned} \text{where } \sigma^{\text{LR}} &= \frac{\beta s}{32\pi} \left[\left(2 + \frac{2}{3}\beta^2\right) (|q^{e_L f_L}|^2 + |q^{e_L f_R}|^2) \right. \\ &\quad \left. + 16 \frac{m_f^2}{s} \text{Re}(q^{e_L f_L} q^{e_L f_R*}) \right], \\ \sigma^{\text{RL}} &= \frac{\beta s}{32\pi} \left[\left(2 + \frac{2}{3}\beta^2\right) (|q^{e_R f_R}|^2 + |q^{e_R f_L}|^2) \right. \\ &\quad \left. + 16 \frac{m_f^2}{s} \text{Re}(q^{e_R f_L} q^{e_R f_R*}) \right]. \quad (20) \end{aligned}$$

Furthermore, considering $m_f \ll \sqrt{s}$ we get

$$\begin{aligned} \sigma^{\text{LR}} &\simeq \frac{s}{12\pi} [|q^{e_L f_L}|^2 + |q^{e_L f_R}|^2], \\ \sigma^{\text{RL}} &\simeq \frac{s}{12\pi} [|q^{e_R f_R}|^2 + |q^{e_R f_L}|^2]. \quad (21) \end{aligned}$$

The statistical error of the cross section $\Delta\sigma^{\text{stat}}(P_{e^-}, P_{e^+})$ is given by

$$\Delta\sigma^{\text{stat}}(P_{e^-}, P_{e^+}) = \frac{\sigma(P_{e^-}, P_{e^+})}{\sqrt{N}}, \quad (22)$$

where $N = \mathcal{L}_{\text{int}}\sigma(P_{e^-}, P_{e^+})$ is the total number of signal events. The deviation of the total fermion pair-production cross section can be written as

To study the effect of beam polarization on the cross section, we consider three polarization choices for the e^- and e^+ beams: (i) Unpolarized case with $P_{e^-} = 0$, $P_{e^+} = 0$; (ii) $P_{e^-} = +0.8$, $P_{e^+} = -0.3$; and (iii) $P_{e^-} = -0.8$, $P_{e^+} = +0.3$. These choices are motivated by the fact that at the ILC, the baseline design foresees at least 80% electron beam polarization at the interaction point, whereas the positron beam can be polarized up to 30% for the undulator positron source (although up to 60% may be possible with the addition of a photon collimator) [55]. In Fig. 7 we show the total production cross section and the corresponding deviation from the SM as a function of \sqrt{s} with these different polarization choices for the processes $e^-e^+ \rightarrow \mu^-\mu^+$ (top row), $b\bar{b}$ (middle row), and $t\bar{t}$ (bottom row) with different x_H values. The SM case has been represented by the solid black line in each panel. Due to the Z' resonance and its interference with the γ and Z -mediated processes, the cross section has a distinct peak at $\sqrt{s} = M_{Z'}$, as can be seen from Fig. 7. We consider $M_{Z'} = 7.5$ TeV and $g' = 0.4$, but larger values of g' will simply broaden the width of the Z' resonance. For the total cross sections, we vary the \sqrt{s} up to 100 TeV to show that even if \sqrt{s} is not exactly at the Z' pole, there could still be large deviations in the total cross section from the SM value.⁴ The deviations in total cross section ($\Delta\sigma$) have been calculated using Eq. (23). These are shown in the lower part of each panel in Fig. 7, but we restrict the x axis only up to $\sqrt{s} = 3$ TeV to show the realistic deviations achievable in the future e^+e^- colliders. Note that $\Delta\sigma$ can be large depending on the choices of x_H , $M_{Z'}$, and g' .

We first consider the $e^-e^+ \rightarrow \mu^-\mu^+$ process which is shown in the top panels of Fig. 7 for different x_H values. As shown in Table IV, for $x_H = -1$ there is no interaction between e_R and Z' , so the cross sections and deviations will have the BSM effect only from q^{LL} . Similarly, for $x_H = -2$ there is no interaction between e_L and Z' ; thus the only BSM effect comes from q^{RR} . These features are manifest in the $e^-e^+ \rightarrow \mu^-\mu^+$ cross sections, which only slightly deviate from the SM case for these x_H values, except exactly at the resonance. On the other hand, for $x_H = 1$ and 2 the BSM contributions will come from all q^{XY} amplitudes to create larger deviations in the total cross sections by widening the resonance.

We perform similar analyses for $e^-e^+ \rightarrow b\bar{b}$ and $e^-e^+ \rightarrow t\bar{t}$ processes which are shown in the middle and bottom panels of Fig. 7, respectively. The nature of the total cross section is the same in these two cases; however, differences appear for different x_H values, as can be seen from Table IV. The $b\bar{b}$ process will be uniquely affected at

⁴This feature was also observed in Ref. [56] in a different model and in the LHC context.

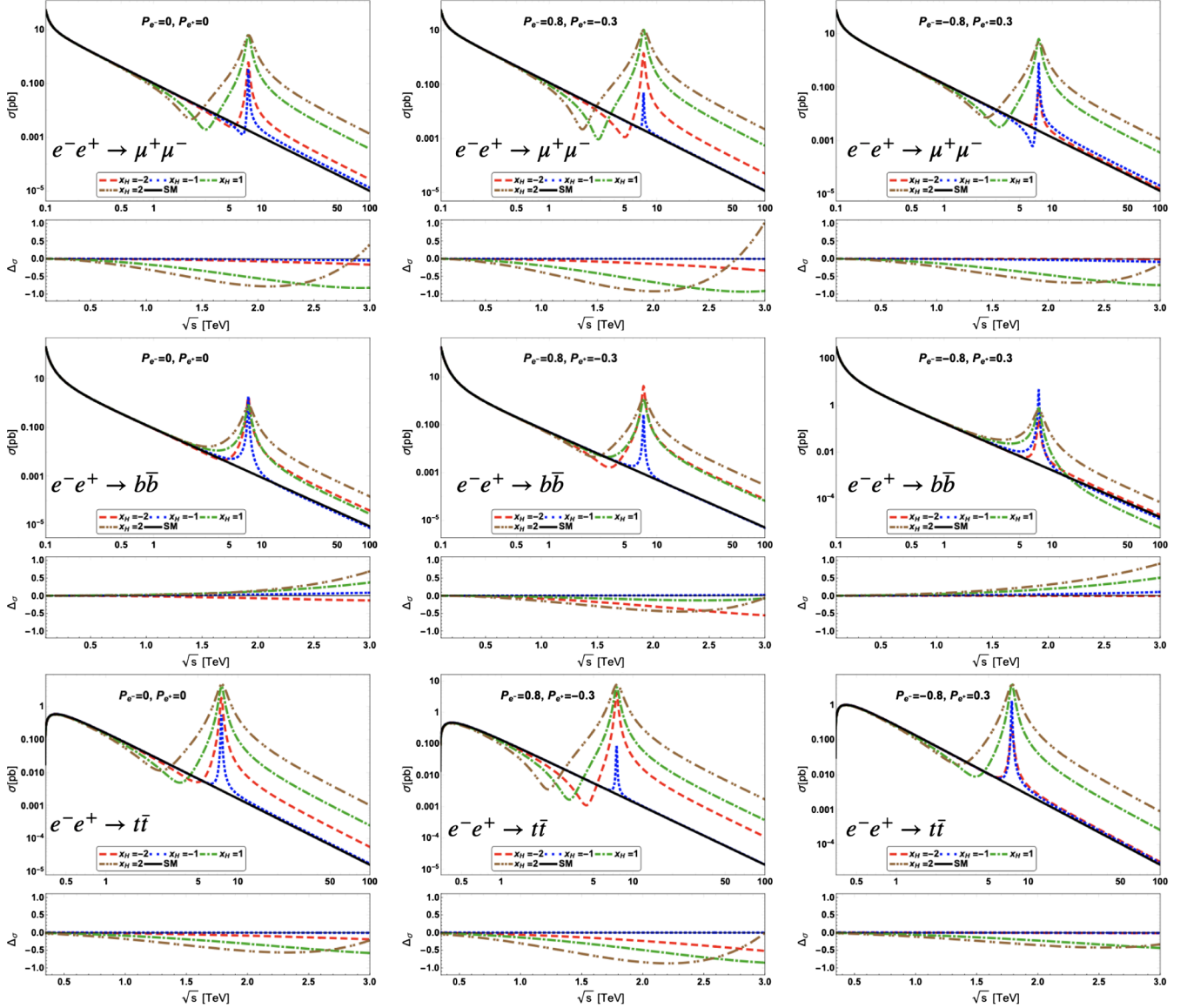


FIG. 7. The total production cross section (upper part of each panel) and the corresponding deviation from the SM (lower part of each panel) for different polarization choices (left to right) as a function of \sqrt{s} considering $M_Z = 7.5$ TeV and $g' = 0.4$.

$x_H = 1$ as there is no interaction between Z' and d_R . As for the $t\bar{t}$ final state, we include the top quark mass of 172 GeV, which is why the cross section goes down when \sqrt{s} approaches this value from above and we only consider $\sqrt{s} \geq 350$ GeV for this process.

As shown in Fig. 7, the deviations in the cross sections from the SM values also depend on the choice of polarization. Taking the $\mu^+\mu^-$ case with unpolarized beams, for example (top left panel), we find that only for $x_H = 2$, the deviation becomes positive at $\sqrt{s} > 2.75$ TeV, whereas it remains negative for the other x_H values up to $\sqrt{s} = 3$ TeV. If we only consider the magnitudes, the deviation is roughly 2.2% for $x_H = -2$ and $x_H = -1$, while it may reach up to 10% and 25% for $x_H = 1$ and $x_H = 2$, respectively, at $\sqrt{s} = 1$ TeV. At smaller $\sqrt{s} = 500$ GeV,

the deviations for $x_H = 2$ and 1 are around 8% and 4%, respectively. On the other hand, at $\sqrt{s} = 3$ TeV, the deviations may reach up to 83% for $x_H = 1$ and 42% for $x_H = 2$.

For $P_e^- = 0.8$, $P_e^+ = -0.3$ (top middle panel), the deviations may reach up to 2% for $x_H = -2$, 5% for $x_H = 1$ and 12% for $x_H = 2$ at $\sqrt{s} = 500$ GeV. For $x_H = 2$, it rapidly decreases between $\sqrt{s} = 2$ and 2.8 TeV, after which it may increase up to 100% at $\sqrt{s} = 3$ TeV. The deviation for $x_H = -1$ is almost negligible up to $\sqrt{s} = 3$ TeV.

For $P_e^- = -0.8$, $P_e^+ = 0.3$ (top right panel), the deviations may be around 10% for $x_H = 2$, 8.5% for $x_H = 1$ at $\sqrt{s} = 500$ GeV. It may reach up to 50% for $\sqrt{s} = 2$ TeV and $x_H = 2$. Similarly for $x_H = 1$ the deviation may reach up to 75% at $\sqrt{s} = 3$ TeV.

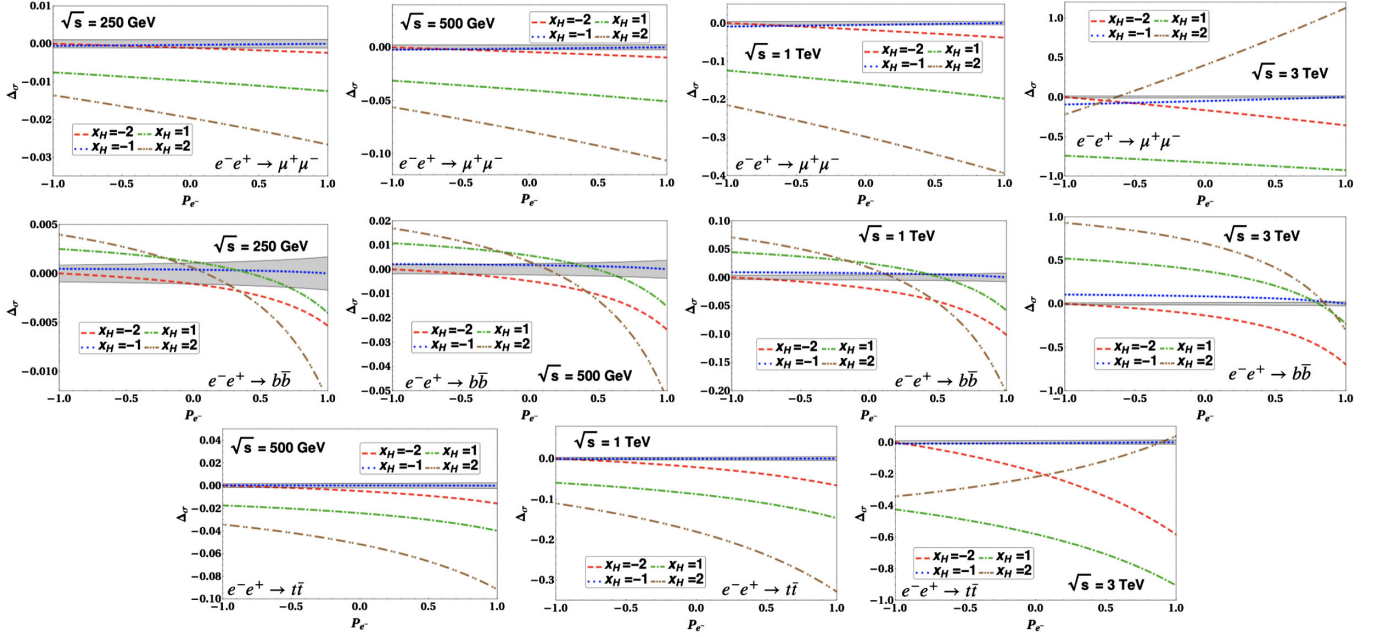


FIG. 8. Deviations of total cross section for the $e^-e^+ \rightarrow f\bar{f}$ process as a function of P_{e^-} keeping $P_{e^+} = 0$ and $M_{Z'} = 7.5$ TeV. The theoretically estimated statistical error is shown by the gray-shaded region. We consider an integrated luminosity $\mathcal{L}_{\text{int}} = 1 \text{ ab}^{-1}$.

The deviations for the $b\bar{b}$ and $t\bar{t}$ processes are shown in the middle and bottom rows of Fig. 7, respectively. Just like the $\mu^+\mu^-$ case, depending on the choices of x_H , \sqrt{s} , and polarizations, the deviations show the nature of the BSM effects of q^{XY} from Table IV.

To see the effect of other polarization choices on the total cross section given by Eq. (23), we now set $P_{e^+} = 0$ and study the variation of the deviation Δ_σ as a function of P_{e^-} in its entire theoretically allowed range of $-1 \leq P_{e^-} \leq 1$, as shown in Fig. 8. The different rows are for $\mu^+\mu^-$ (top), $b\bar{b}$ (middle), and $t\bar{t}$ (bottom), whereas the different columns (from left to right) are for $\sqrt{s} = 250$ GeV, 500 GeV, 1 TeV, and 3 TeV. For the $t\bar{t}$ case, we do not have the $\sqrt{s} = 250$ GeV option because it is below the $t\bar{t}$ threshold. Here we have used $\mathcal{L}_{\text{int}} = 1 \text{ ab}^{-1}$, $M_{Z'} = 7.5$ TeV, and $g' = 0.4$. In each panel, we also show the theoretically estimated statistical error (gray-shaded region), defined as

$$\Delta_\sigma^{\text{stat}}(P_{e^-}, P_{e^+}) = \sqrt{2} \frac{\Delta\sigma^{\text{stat}}(P_{e^-}, P_{e^+})}{\sigma(P_{e^-}, P_{e^+})} = \frac{\sqrt{2}}{\sqrt{N}}. \quad (24)$$

Thus the statistical error decreases with increasing cross sections (or increasing \sqrt{s}) for a fixed luminosity.

In the $\mu^+\mu^-$ process Δ_σ can reach up to 2.7% for $P_{e^-} = 0.8$ and 1.5% for $P_{e^-} = -0.8$ at $\sqrt{s} = 250$ GeV with $x_H = 2$. The deviations for other x_H are comparatively small. At $\sqrt{s} = 500$ GeV these values become 11% and 6% at $P_{e^-} = 0.8$ and -0.8 , respectively, for $x_H = 2$. At the same \sqrt{s} these values become 2.8% and 2.5%, respectively, for $x_H = 1$. These deviations gradually increase with \sqrt{s} ,

while the statistical error decreases, as can be seen by comparing the different columns in Fig. 8. We find that for some of the x_H and P_{e^-} values, the deviations can be larger than the statistical error, and hence, observable at future colliders.

At $\sqrt{s} = 250$ GeV, Δ_σ for $b\bar{b}$ is roughly below 1% for all x_H when $P_{e^-} = 0.8$ and $P_{e^-} = -0.8$. The deviations increase with \sqrt{s} and can be within 1%–4% for different x_H except for $x_H = -2$ at $P_{e^-} = 0.8$ considering $\sqrt{s} = 500$ GeV. Δ_σ increases roughly by a factor of 3 for $P_{e^-} = 0.8$ at $\sqrt{s} = 1$ TeV. Similar behavior can be observed at $\sqrt{s} = 3$ TeV; however, the deviations can become very large depending on the x_H and/or P_{e^-} values. In case of $t\bar{t}$ production, Δ_σ at $\sqrt{s} = 500$ GeV can be 7% for $x_H = 2$ and 2.5% for $x_H = 1$ at $P_{e^-} = 0.8$. At $P_{e^-} = -0.8$ for the same charges Δ_σ can be 3.5% and 1.8%, respectively. The results for $x_H = -2$ are below 1%.

C. Forward-backward asymmetry (\mathcal{A}_{FB})

The integrated forward-backward (FB) asymmetry (\mathcal{A}_{FB}) is an interesting feature of this model which can be observed at e^-e^+ colliders. It is defined as [57–59]

$$\mathcal{A}_{\text{FB}}(P_{e^-}, P_{e^+}) = \frac{\sigma_F(P_{e^-}, P_{e^+}) - \sigma_B(P_{e^-}, P_{e^+})}{\sigma_F(P_{e^-}, P_{e^+}) + \sigma_B(P_{e^-}, P_{e^+})}, \quad (25)$$

where the cross sections in the forward (σ_F) and backward (σ_B) directions can be defined by taking the limits of the θ integration in Eq. (18) as $[0, +\cos\theta_{\text{max}}]$ and $[-\cos\theta_{\text{max}}, 0]$,

respectively. For $m_f \ll \sqrt{s}$ and $\cos \theta_{\max} = 1$, Eq. (25) is reduced to

$$\mathcal{A}_{\text{FB}}(P_{e^-}, P_{e^+}) \simeq \frac{3B_1 - B_2}{4B_1 + B_2}, \quad (26)$$

where the coupling dependent quantities B_1 and B_2 can be defined as

$$B_1 = (1 + P_{\text{eff}})|q^{e_R f_R}|^2 + (1 - P_{\text{eff}})|q^{e_L f_L}|^2, \quad (27)$$

$$B_2 = (1 + P_{\text{eff}})|q^{e_R f_L}|^2 + (1 - P_{\text{eff}})|q^{e_L f_R}|^2. \quad (28)$$

The integrated FB asymmetry from Eq. (25) is shown in Fig. 9 for $M_{Z'} = 7.5$ TeV as a function of \sqrt{s} for $\mu^+\mu^-$ (top panel), $b\bar{b}$ (middle panel), and $t\bar{t}$ (bottom panel). We consider three combinations of polarizations for the e^- and e^+ as before. Taking $x_H = -2, -1, 1$, and 2 we compare \mathcal{A}_{FB} in the presence of Z' with that in the SM. In this analysis \mathcal{A}_{FB} is an important observable in s -channel scattering. For different choices of x_H , \mathcal{A}_{FB} contains the BSM effect from q^{XY} according to Table IV. These are clearly affected by the choice of x_H . For $e^-e^+ \rightarrow \mu^+\mu^-$, the integrated FB asymmetries for $x_H = -2$ and -1 can be, respectively, written as

$$\mathcal{A}_{\text{FB}}^{x_H=-2}(P_{e^-}, P_{e^+}) \simeq \frac{3(1 + P_{\text{eff}})\{|q^{e_R \mu_R}|^2 - |q_{\text{SM}}^{e_R \mu_L}|^2\} + (1 - P_{\text{eff}})\{|q_{\text{SM}}^{e_L \mu_L}|^2 - |q_{\text{SM}}^{e_L f_R}|^2\}}{4(1 + P_{\text{eff}})\{|q^{e_R \mu_R}|^2 + |q_{\text{SM}}^{e_R \mu_L}|^2\} + (1 - P_{\text{eff}})\{|q_{\text{SM}}^{e_L \mu_L}|^2 + |q_{\text{SM}}^{e_L \mu_R}|^2\}}, \quad (29)$$

$$\mathcal{A}_{\text{FB}}^{x_H=-1}(P_{e^-}, P_{e^+}) \simeq \frac{3(1 + P_{\text{eff}})\{|q_{\text{SM}}^{e_R \mu_R}|^2 - |q_{\text{SM}}^{e_R \mu_L}|^2\} + (1 - P_{\text{eff}})\{|q_{\text{SM}}^{e_L \mu_L}|^2 - |q_{\text{SM}}^{e_L \mu_R}|^2\}}{4(1 + P_{\text{eff}})\{|q_{\text{SM}}^{e_R \mu_R}|^2 + |q_{\text{SM}}^{e_R f_L}|^2\} + (1 - P_{\text{eff}})\{|q_{\text{SM}}^{e_L \mu_L}|^2 + |q_{\text{SM}}^{e_L \mu_R}|^2\}}. \quad (30)$$

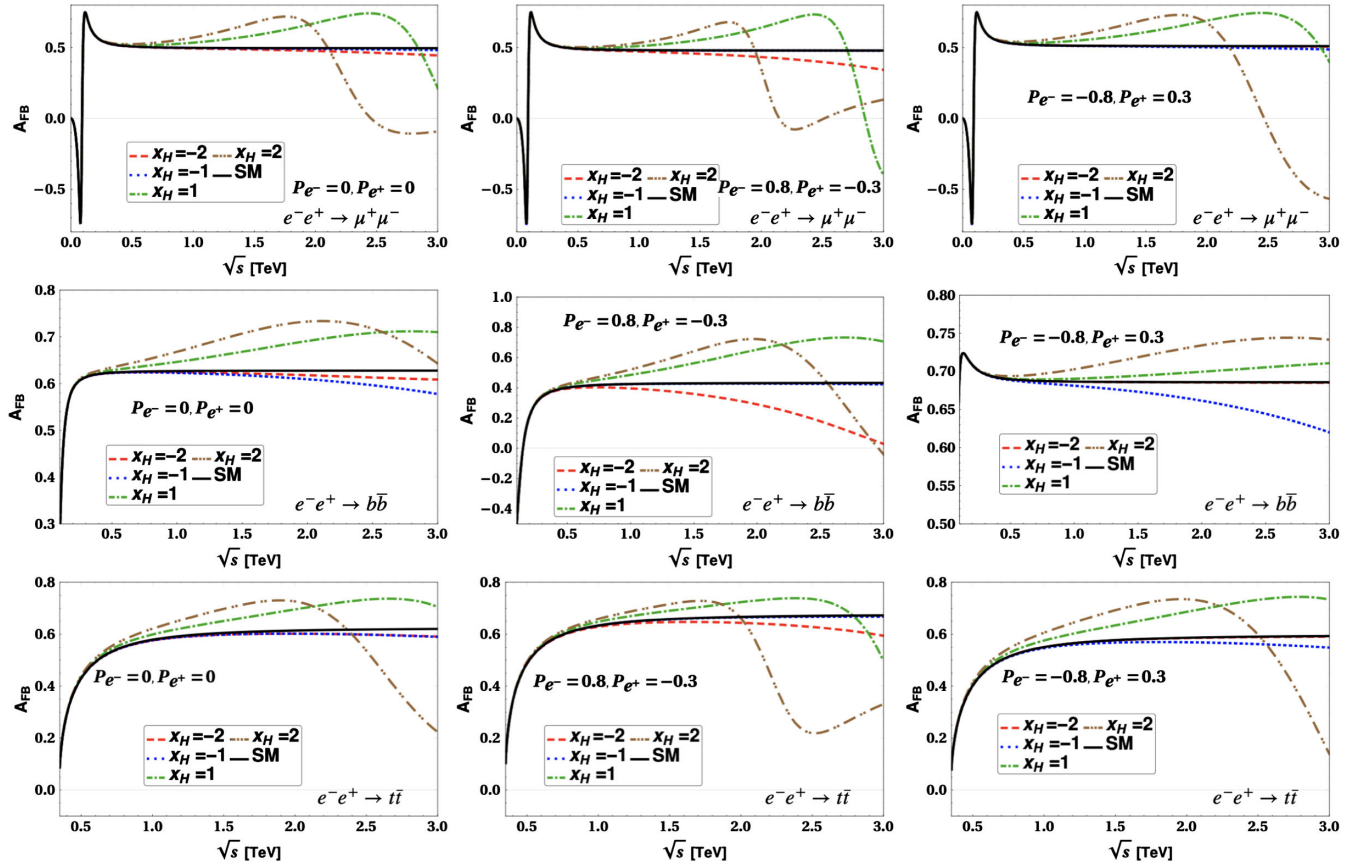


FIG. 9. The integrated FB asymmetry for different choices of x_H as a function of the center of mass energy for $e^-e^+ \rightarrow f\bar{f}$ process with $\mu^+\mu^-$ (top row), $b\bar{b}$ (middle row), and $t\bar{t}$ (bottom row). The columns correspond to three sets of polarizations of incoming electron and positron beams. We have chosen $M_{Z'} = 7.5$ TeV and $g' = 0.4$. The SM result is shown by the solid black line in each case.

For other x_H values, the BSM effects come from all q^{XY} combinations. In Eqs. (29) and (30), the term SM denotes the SM effects from $\{Z, \gamma\}$ and the corresponding interferences with the BSM. Note that for $x_H = -2$ and -1 the BSM effect in \mathcal{A}_{FB} is small for $\mu^- \mu^+$ process compared to the SM (represented by solid black line) in the top panel of Fig. 9. For the other two charges $x_H = 1$ and 2, \mathcal{A}_{FB} is comparatively higher than the SM result due to the effects of all q^{XY} for different polarizations. \mathcal{A}_{FB} depends on the quantities $(1 - P_{\text{eff}})$ and $(1 + P_{\text{eff}})$ which will be either

$$\mathcal{A}_{\text{FB}}^{x_H=-1}(P_{e^-}, P_{e^+}) \simeq \frac{3(1 + P_{\text{eff}})\{|q_{\text{SM}}^{e_R b_R}|^2 - |q_{\text{SM}}^{e_R b_L}|^2\} + (1 - P_{\text{eff}})\{|q_{\text{SM}}^{e_L b_L}|^2 - |q_{\text{SM}}^{e_L b_R}|^2\}}{4(1 + P_{\text{eff}})\{|q_{\text{SM}}^{e_R b_R}|^2 + |q_{\text{SM}}^{e_R b_L}|^2\} + (1 - P_{\text{eff}})\{|q_{\text{SM}}^{e_L b_L}|^2 + |q_{\text{SM}}^{e_L b_R}|^2\}}, \quad (31)$$

$$\mathcal{A}_{\text{FB}}^{x_H=1}(P_{e^-}, P_{e^+}) \simeq \frac{3(1 + P_{\text{eff}})\{|q_{\text{SM}}^{e_R b_R}|^2 - |q_{\text{SM}}^{e_R b_L}|^2\} + (1 - P_{\text{eff}})\{|q_{\text{SM}}^{e_L b_L}|^2 - |q_{\text{SM}}^{e_L b_R}|^2\}}{4(1 + P_{\text{eff}})\{|q_{\text{SM}}^{e_R b_R}|^2 + |q_{\text{SM}}^{e_R b_L}|^2\} + (1 - P_{\text{eff}})\{|q_{\text{SM}}^{e_L b_L}|^2 + |q_{\text{SM}}^{e_L b_R}|^2\}}. \quad (32)$$

In this case $x_H = -2$ will affect the interaction between electron and Z' which will be reflected in the nature of \mathcal{A}_{FB} . The nature of the asymmetries for $b\bar{b}$ process is shown in the middle panels of Fig. 9 for all x_H and different polarizations. For the top quark pair production all q^{XY} contribute for $x_H = 2$. The rest of the contributions can be obtained from Eqs. (29)–(32) depending on x_H values. The nature of the FB asymmetry for the $t\bar{t}$ process is shown in the bottom panels of Fig. 9 for different values of x_H and different sets of polarizations.

greater or less than 1; however, for our choice of nonzero polarizations $(1 - P_{\text{eff}})$ and $(1 + P_{\text{eff}})$ are always positive. Depending on the choice of x_H , \mathcal{A}_{FB} could be greater or less than the results of SM.

For the $e^- e^+ \rightarrow b\bar{b}$ process, we notice that for $x_H = -1$ the BSM contributions come from q^{LL} and q^{LR} in the FB asymmetry, whereas for $x_H = 1$ the BSM contributions come from q^{LL} and q^{RL} . The expressions for these charges can be written as

The deviation of the FB asymmetry from the SM result can be defined as

$$\Delta_{\mathcal{A}_{\text{FB}}} = \frac{\mathcal{A}_{\text{FB}}^{U(1)_X}}{\mathcal{A}_{\text{FB}}^{\text{SM}}} - 1. \quad (33)$$

$\Delta_{\mathcal{A}_{\text{FB}}}$ is shown in Fig. 10 for $\mu^- \mu^+$ (top panel), $b\bar{b}$ (middle panel), and $t\bar{t}$ (bottom panel) using $M_{Z'} = 7.5$ TeV and keeping $P_{e^+} = 0$, while varying P_{e^-} from

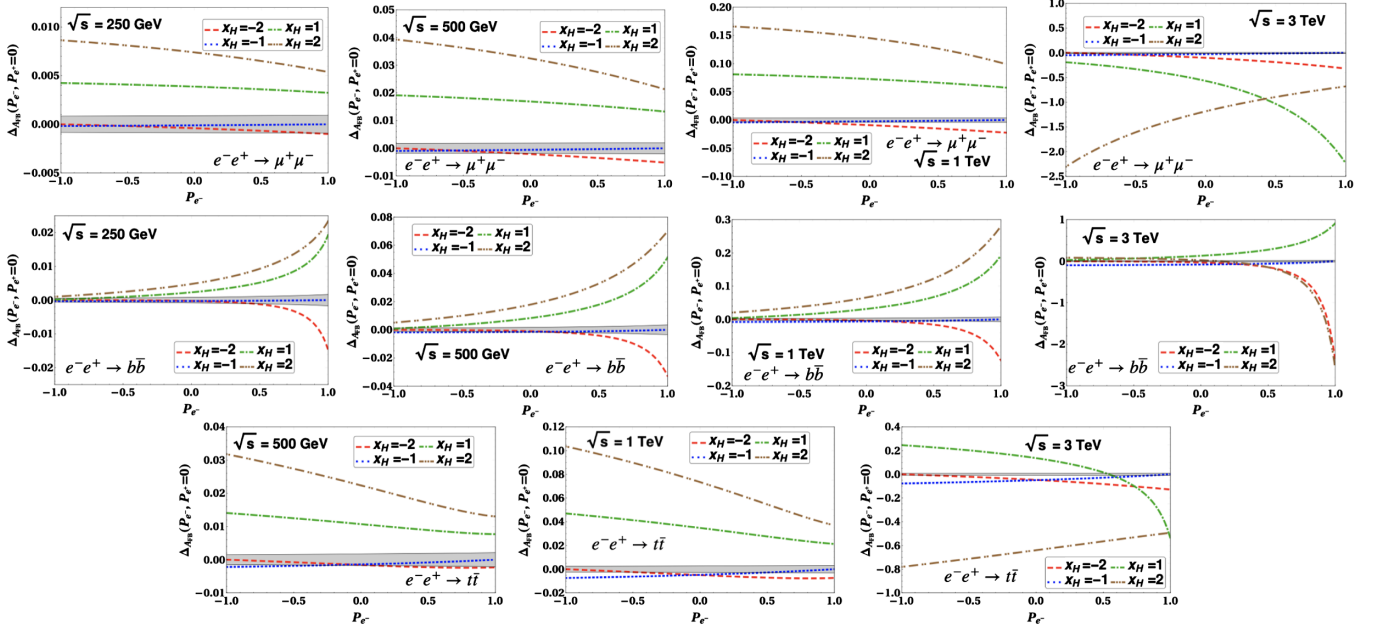


FIG. 10. The deviation in the integrated FB asymmetry as a function of P_{e^-} for $e^- e^+ \rightarrow f\bar{f}$ process taking $P_{e^+} = 0$ for $M_{Z'} = 7.5$ TeV. The theoretically estimated statistical error has been represented by the gray-shaded band. The integrated luminosity is taken to be $\mathcal{L}_{\text{int}} = 1 \text{ ab}^{-1}$.

0 to 1. The theoretically estimated statistical error represented by the gray-shaded band has been calculated as

$$\Delta \mathcal{A}_{\text{FB}}^{\text{stat}} = \frac{2\sqrt{N_F N_B}}{(N_F + N_B)(\sqrt{N_F} - \sqrt{N_B})} \mathcal{A}_{\text{FB}}, \quad (34)$$

where $N_{F(B)} = \mathcal{L}_{\text{int}} \sigma_{F(B)}(P_{e^-}, P_{e^+})$ is the number of events in the forward (backward) direction. The different columns correspond to $\sqrt{s} = 250$ GeV (except for $t\bar{t}$), 500 GeV, 1 TeV, and 3 TeV. The nature of the deviations shown here can be understood from Eqs. (29)–(32). The BSM contributions in differential FB asymmetry for different fermions for different x_H are guided by Table IV.

We find that at $\sqrt{s} = 250$ GeV the deviations in FB asymmetry from the SM in the case of $\mu^-\mu^+$ is less than 1% for all x_H . For all \sqrt{s} , the cases $x_H = -2$ and -1 are within the theoretically estimated statistical error. Even for $\sqrt{s} = 3$ TeV and $P_{e^-} = 0.8$ the deviation is roughly 3% for $x_H = -2$. In the case of $\sqrt{s} = 500$ GeV for $P_{e^-} = -0.8$ the deviation is 1.9% and that for $P_{e^+} = 0.8$ is 1.8% for $x_H = 1$. The deviations for $x_H = 2$ are 3.9% and 3.4% for $P_{e^-} = -0.8$ and $P_{e^+} = 0.8$, respectively. The deviation for $x_H = -2$ is nearly 2% for $P_{e^-} = 0.8$ at $\sqrt{s} = 1$ TeV. For $x_H = 1$ the deviations are 8% and 7% for $P_{e^-} = -0.8$ and $P_{e^+} = 0.8$, respectively, at $\sqrt{s} = 1$ TeV. At $\sqrt{s} = 1$ TeV the deviation for $x_H = 2$ at $P_{e^-} = -0.8$ is roughly 16.5% and at $P_{e^-} = 0.8$ the deviation is roughly 13%. The

deviations for $x_H = 2$ and 1 at $\sqrt{s} = 3$ TeV are very large compared to the other choices of \sqrt{s} .

Studying the $b\bar{b}$ process we find the deviation is small at $\sqrt{s} = 250$ GeV for $P_{e^-} = -0.8$ and the deviation at $P_{e^-} = 0.8$ is around 2% for $x_H = 2$. The deviation at $P_{e^-} = 0.8$ is below 2% for $x_H = -2$. For $x_H = 1$ and $x_H = 2$ the deviations are around 3% and 5.5% respectively for $\sqrt{s} = 500$ GeV at $P_{e^-} = 0.8$. The deviations for $x_H = -2, 1$ and 2 are enhanced by orders of magnitude at $\sqrt{s} = 1$ and 3 TeV. In case of $t\bar{t}$ we notice that the deviation is large at $P_{e^-} = -0.8$ for different x_H . At $\sqrt{s} = 500$ GeV the deviations are roughly 3% for $x_H = 2$ and 1.4% for $x_H = 1$. The deviations increase with \sqrt{s} by some factor up to an order of magnitude depending on x_H and P_{e^-} .

D. Differential left-right asymmetry ($\mathcal{A}_{\text{LR}}(\cos\theta)$)

The left-right (LR) asymmetry (\mathcal{A}_{LR}) is another important observable which can be tested at the e^-e^+ colliders [57,58,60–62]. The differential \mathcal{A}_{LR} is given by

$$\mathcal{A}_{\text{LR}}(\cos\theta) = \frac{\frac{d\sigma_{\text{LR}}}{d\cos\theta}(\cos\theta) - \frac{d\sigma_{\text{RL}}}{d\cos\theta}(\cos\theta)}{\frac{d\sigma_{\text{LR}}}{d\cos\theta}(\cos\theta) + \frac{d\sigma_{\text{RL}}}{d\cos\theta}(\cos\theta)}, \quad (35)$$

where $\frac{d\sigma_{\text{LR}}}{d\cos\theta}$ and $\frac{d\sigma_{\text{RL}}}{d\cos\theta}$ are given in Eqs. (14) and (15), respectively. For $m_f \ll \sqrt{s}$, Eq. (35) reduces to

$$\mathcal{A}_{\text{LR}}(\cos\theta) \simeq \frac{(1 + \cos\theta)^2(|q^{eLfL}|^2 - |q^{eRfR}|^2) + (1 - \cos\theta)^2(|q^{eLfR}|^2 - |q^{eRfL}|^2)}{(1 + \cos\theta)^2(|q^{eLfL}|^2 + |q^{eRfR}|^2) + (1 - \cos\theta)^2(|q^{eLfR}|^2 + |q^{eRfL}|^2)}. \quad (36)$$

The observable differential \mathcal{A}_{LR} in terms of the e^\pm polarizations can be written as

$$\mathcal{A}_{\text{LR}}(P_{e^-}, P_{e^+}, \cos\theta) = \frac{\frac{d\sigma}{d\cos\theta}(P_{e^-}, P_{e^+}, \cos\theta) - \frac{d\sigma}{d\cos\theta}(-P_{e^-}, -P_{e^+}, \cos\theta)}{\frac{d\sigma}{d\cos\theta}(P_{e^-}, P_{e^+}, \cos\theta) + \frac{d\sigma}{d\cos\theta}(-P_{e^-}, -P_{e^+}, \cos\theta)}. \quad (37)$$

for $P_{e^-} < 0$ and $|P_{e^-}| > |P_{e^+}|$. Hence we find that Eq. (37) is related to Eq. (36) by

$$\mathcal{A}_{\text{LR}}(\cos\theta) = \frac{1}{P_{\text{eff}}} \mathcal{A}_{\text{LR}}(P_{e^-}, P_{e^+}, \cos\theta). \quad (38)$$

The nature of differential LR asymmetry from Eq. (37) is shown in Fig. 11 for $\mu^+\mu^-$ (top panel), $b\bar{b}$ (middle panel), and $t\bar{t}$ (bottom panel) using $M_{Z'} = 7.5$ TeV as a function of $\cos\theta$ for $\sqrt{s} = 250$ GeV (except $t\bar{t}$), 500 GeV, 1 TeV, and

3 TeV, respectively. We estimate the asymmetry parameter for the $U(1)_X$ scenario considering $x_H = -2, -1, 1$, and 2 and present them along with the SM result (solid black line). The LR asymmetry depends on x_H through the interactions between the charged fermions and Z' as shown in Table IV. According to that, the differential LR asymmetry for $x_H = -2$ and -1 for the $e^-e^+ \rightarrow \mu^+\mu^-$ process from Eq. (36) can be written as

$$\mathcal{A}_{\text{LR}}(\cos\theta)_{x_H=-2} \simeq \frac{(1 + \cos\theta)^2(|q_{\text{SM}}^{eL\mu L}|^2 - |q_{\text{SM}}^{eR\mu R}|^2) + (1 - \cos\theta)^2(|q_{\text{SM}}^{eL\mu R}|^2 - |q_{\text{SM}}^{eR\mu L}|^2)}{(1 + \cos\theta)^2(|q_{\text{SM}}^{eL\mu L}|^2 + |q_{\text{SM}}^{eR\mu R}|^2) + (1 - \cos\theta)^2(|q_{\text{SM}}^{eL\mu R}|^2 + |q_{\text{SM}}^{eR\mu L}|^2)}, \quad (39)$$

$$\mathcal{A}_{\text{LR}}(\cos\theta)_{x_H=-1} \simeq \frac{(1 + \cos\theta)^2(|q_{\text{SM}}^{eL\mu L}|^2 - |q_{\text{SM}}^{eR\mu R}|^2) + (1 - \cos\theta)^2(|q_{\text{SM}}^{eL\mu R}|^2 - |q_{\text{SM}}^{eR\mu L}|^2)}{(1 + \cos\theta)^2(|q_{\text{SM}}^{eL\mu L}|^2 + |q_{\text{SM}}^{eR\mu R}|^2) + (1 - \cos\theta)^2(|q_{\text{SM}}^{eL\mu R}|^2 + |q_{\text{SM}}^{eR\mu L}|^2)}. \quad (40)$$

The results are shown in the top panels of Fig. 11.

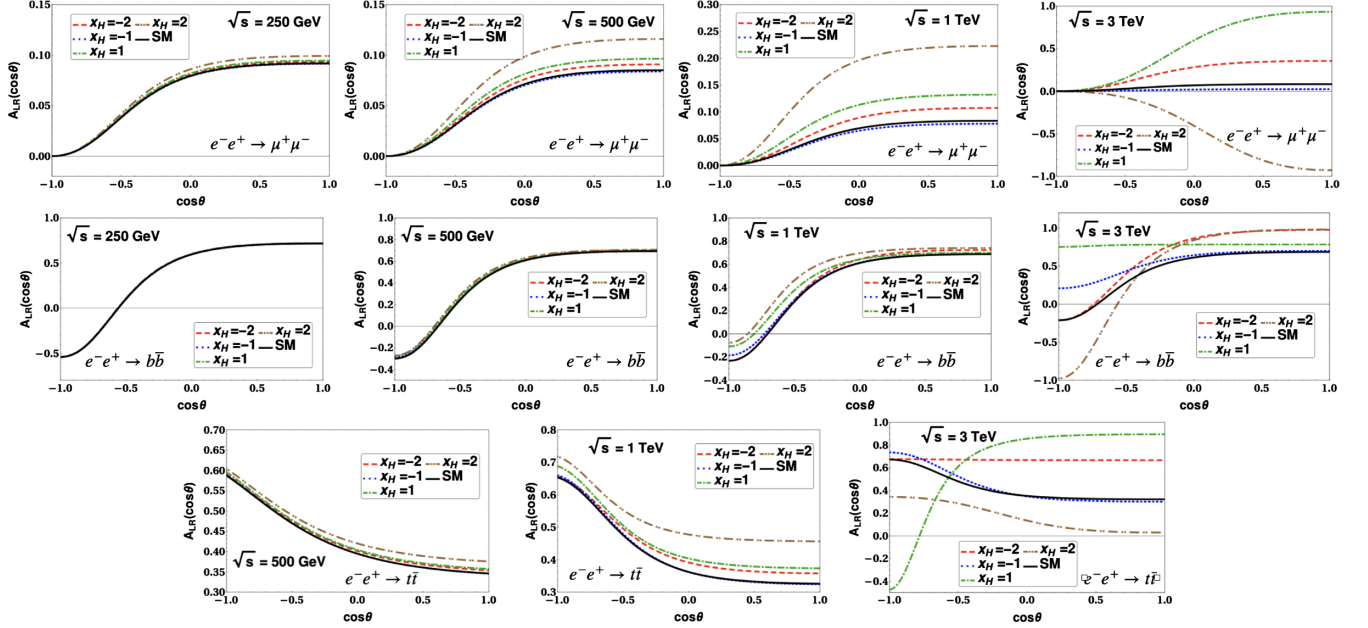


FIG. 11. The differential LR asymmetry for $e^-e^+ \rightarrow f\bar{f}$ process as a function of $\cos\theta$ for $M_{Z'} = 7.5$ TeV. The contribution from the SM has been represented by the black solid line.

For the $b\bar{b}$ process we find the BSM contributions for different x_H in the differential LR asymmetry in terms of q^{XY} following Table IV. Using Eq. (37), the differential LR asymmetry of this process for $x_H = -1$ and 1 can be written as

$$\mathcal{A}_{\text{LR}}(\cos\theta)^{x_H=-1} \simeq \frac{(1 + \cos\theta)^2(|q_{e_L b_L}^{e_L}|^2 - |q_{\text{SM}}^{e_R b_R}|^2) + (1 - \cos\theta)^2(|q_{e_L b_R}^{e_L}|^2 - |q_{\text{SM}}^{e_R b_L}|^2)}{(1 + \cos\theta)^2(|q_{e_L b_L}^{e_L}|^2 + |q_{\text{SM}}^{e_R b_R}|^2) + (1 - \cos\theta)^2(|q_{e_L b_R}^{e_L}|^2 + |q_{\text{SM}}^{e_R b_L}|^2)}, \quad (41)$$

$$\mathcal{A}_{\text{LR}}(\cos\theta)^{x_H=1} \simeq \frac{(1 + \cos\theta)^2(|q_{e_L b_L}^{e_L}|^2 - |q_{\text{SM}}^{e_R b_R}|^2) + (1 - \cos\theta)^2(|q_{\text{SM}}^{e_L b_R}|^2 - |q_{e_R b_L}^{e_R}|^2)}{(1 + \cos\theta)^2(|q_{e_L b_L}^{e_L}|^2 + |q_{\text{SM}}^{e_R b_R}|^2) + (1 - \cos\theta)^2(|q_{\text{SM}}^{e_L b_R}|^2 + |q_{e_R b_L}^{e_R}|^2)}. \quad (42)$$

The results are shown in the middle panels of Fig. 11. Similarly, we study the LR asymmetry for $e^-e^+ \rightarrow t\bar{t}$ process according to Table IV and Eq. (37) for different x_H . We find that for all three final states, the size of the differential LR asymmetry increases with the increase in \sqrt{s} from the SM prediction (solid black line). In the $U(1)_X$ case, it is governed by different couplings of the left- and right-handed fermions with Z' , as summarized in Table IV.

The amount of deviation from the SM in the differential asymmetries can be defined as

$$\Delta_{\mathcal{A}_{\text{LR}}}(\cos\theta) = \frac{\mathcal{A}_{\text{LR}}^{U(1)_X}(\cos\theta)}{\mathcal{A}_{\text{LR}}^{\text{SM}}(\cos\theta)} - 1. \quad (43)$$

We show these deviations using $M_{Z'} = 7.5$ TeV in Fig. 12 for $\mu^+\mu^-$ (top panel), $b\bar{b}$ (middle panel), and $t\bar{t}$ (bottom panel) as a function of $\cos\theta$. We use $\sqrt{s} = 250$ GeV (except $t\bar{t}$), 500 GeV, 1 TeV, and 3 TeV and present the results for $x_H = -2, -1, 1$, and 2. The theoretically

estimated statistical error, shown as the gray-shaded band is estimated from

$$\Delta \mathcal{A}_{\text{LR}}^{\text{stat}} = \frac{2\sqrt{N_{\text{LR}}N_{\text{RL}}}}{(N_{\text{LR}} + N_{\text{RL}})(\sqrt{N_{\text{LR}}} - \sqrt{N_{\text{RL}}})} \mathcal{A}_{\text{LR}}, \quad (44)$$

where $N_{\text{LR}} = \mathcal{L}_{\text{int}}\sigma_{\text{LR}}$ and $N_{\text{RL}} = \mathcal{L}_{\text{int}}\sigma_{\text{RL}}$.

From Fig. 12, we find that the deviation in differential LR asymmetry for $e^-e^+ \rightarrow \mu^+\mu^-$ process for $x_H = -2$ is slightly above the theoretically estimated statistical error for $\cos\theta > 0.37$; however, for $x_H = -1$ it is within the range of the statistical error. For $x_H = 1$ and 2, the deviations vary between 5%–3% and 10%–8%, respectively, for $-1 \leq \cos\theta \leq 1$. The deviations increase with \sqrt{s} . The differential LR asymmetry is negative for $x_H = 2$ at $\sqrt{s} = 3$ TeV which is reflected in the deviation of the differential LR asymmetry as well.

The deviation in differential LR asymmetry as a function of $\cos\theta$ for the process $e^-e^+ \rightarrow b\bar{b}$ has a singularity. This is because the differential LR asymmetry for the $b\bar{b}$ process in

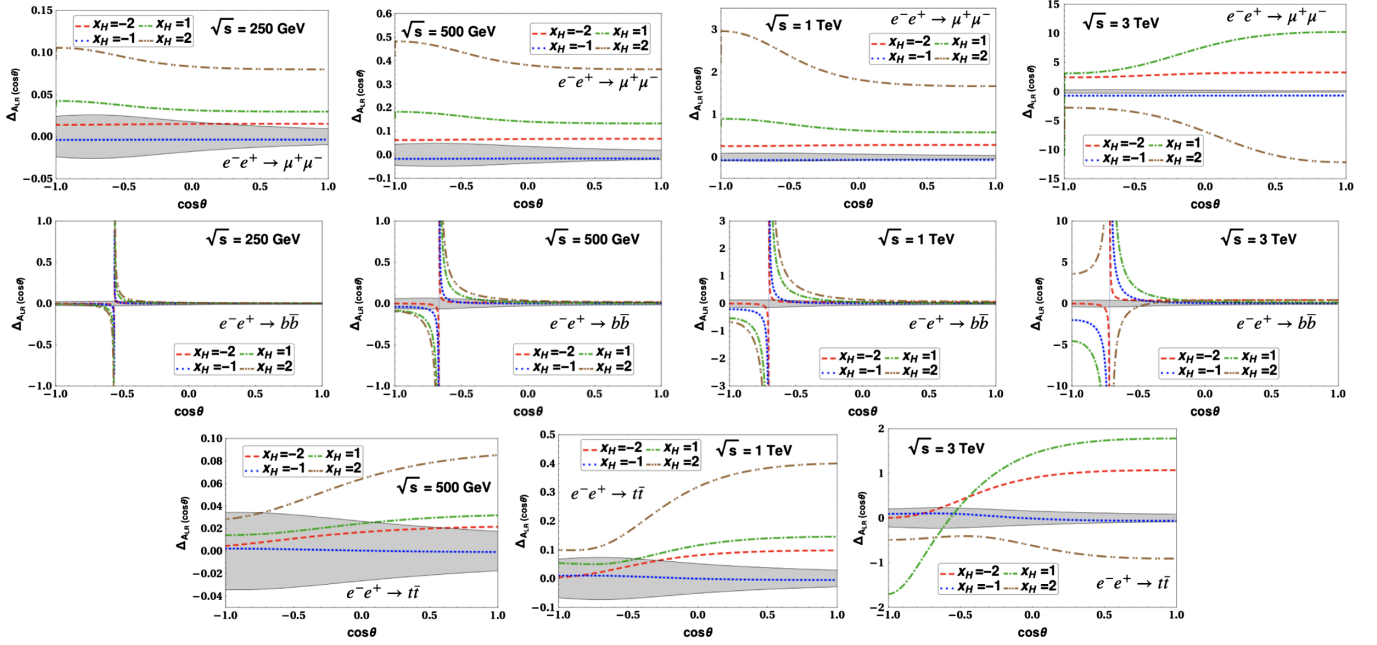


FIG. 12. The deviations in the differential LR asymmetry for $e^-e^+ \rightarrow f\bar{f}$ process as a function of $\cos\theta$ for $M_{Z'} = 7.5$ TeV. The theoretically estimated statistical error has been represented by the gray-shaded band. The integrated luminosity is taken as $\mathcal{L}_{\text{int}} = 1 \text{ ab}^{-1}$.

the SM vanishes at $\cos\theta \simeq -0.5594$ for $\sqrt{s} = 250$ GeV. Similar behavior can be observed at $\cos\theta \simeq -0.668$ for $\sqrt{s} = 500$ GeV, $\cos\theta \simeq -0.7042$ for $\sqrt{s} = 1$ TeV, and $\cos\theta \simeq -0.7162$ for $\sqrt{s} = 3$ TeV for the SM. Around these angles the differential LR asymmetry for the $b\bar{b}$ process is very high and rapidly grows towards 100%. As for the $t\bar{t}$ process, at $\sqrt{s} = 500$ GeV the differential LR asymmetry is greater than 6% at $x_H = 2$ for $\cos\theta > 0$. The deviation is around 3% for $x_H = 1$ for $\cos\theta > 0$. For the rest of the choices of x_H it stays within the theoretically estimated statistical error. With the increase in \sqrt{s} , the deviation

increases with $\cos\theta$; however, $x_H = -1$ stays within the theoretically estimated statistical error throughout.

E. Integrated left-right asymmetry (\mathcal{A}_{LR})

We also calculate the integrated \mathcal{A}_{LR} by integrating Eq. (35) over the scattering angle:

$$\mathcal{A}_{\text{LR}} = \frac{\sigma_{\text{LR}}^{\text{LR}} - \sigma_{\text{LR}}^{\text{RL}}}{\sigma_{\text{LR}}^{\text{LR}} + \sigma_{\text{LR}}^{\text{RL}}}. \quad (45)$$

In terms of the gauge couplings of the fermions, we can write Eq. (45) as

$$\mathcal{A}_{\text{LR}} = \frac{(1 + \frac{1}{3}\beta^2)[(|q^{eLfL}|^2 + |q^{eLfR}|^2) - (|q^{eRfR}|^2 + |q^{eRfL}|^2)] + 8\frac{m_f^2}{s}[\text{Re}(q^{eLfL}q^{eLfR*}) - \text{Re}(q^{eRfR}q^{eRfL*})]}{(1 + \frac{1}{3}\beta^2)[(|q^{eLfL}|^2 + |q^{eLfR}|^2) + (|q^{eRfR}|^2 + |q^{eRfL}|^2)] + 8\frac{m_f^2}{s}[\text{Re}(q^{eLfL}q^{eLfR*}) + \text{Re}(q^{eRfR}q^{eRfL*})]}. \quad (46)$$

In the limit $m_f \ll \sqrt{s}$, Eq. (46) is reduced to

$$\mathcal{A}_{\text{LR}} \simeq \frac{(|q^{eLfL}|^2 + |q^{eLfR}|^2) - (|q^{eRfR}|^2 + |q^{eRfL}|^2)}{(|q^{eLfL}|^2 + |q^{eLfR}|^2) + (|q^{eRfR}|^2 + |q^{eRfL}|^2)}. \quad (47)$$

The observable integrated \mathcal{A}_{LR} as a function of the electron and positron beam polarizations is given by

$$\mathcal{A}_{\text{LR}}(P_{e^-}, P_{e^+}) = \frac{\sigma(P_{e^-}, P_{e^+}) - \sigma(-P_{e^-}, -P_{e^+})}{\sigma(P_{e^-}, P_{e^+}) + \sigma(-P_{e^-}, -P_{e^+})}, \quad (48)$$

for $P_{e^-} < 0$ and $|P_{e^-}| > |P_{e^+}|$. This is related to Eq. (45) by

$$\mathcal{A}_{\text{LR}} = \frac{1}{P_{\text{eff}}} \mathcal{A}_{\text{LR}}(P_{e^-}, P_{e^+}). \quad (49)$$

The integrated LR asymmetries from Eq. (46) for $e^-e^+ \rightarrow \mu^+\mu^-$, $b\bar{b}$, and $t\bar{t}$ as a function of \sqrt{s} are shown in Fig. 13 with $M_{Z'} = 7.5$ TeV and for different x_H values. The BSM contributions depending on the x_H charges are governed according to Table IV. The SM value is shown by the solid black line. The integrated LR

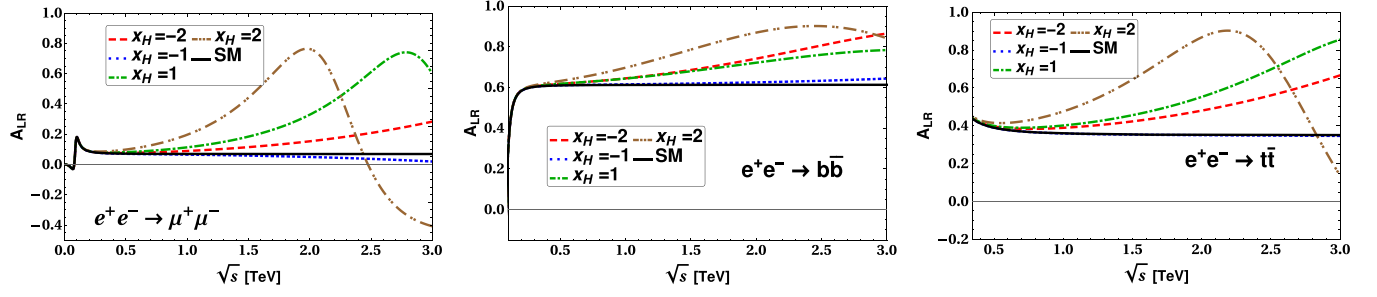


FIG. 13. The integrated LR asymmetry for the process $e^-e^+ \rightarrow f\bar{f}$ as a function of \sqrt{s} for $M_{Z'} = 7.5$ TeV. The contribution from the SM has been represented by the black solid line.

asymmetry for $e^-e^+ \rightarrow \mu^+\mu^-$ process and $x_H = -2$ and -1 can be written as

$$\mathcal{A}_{\text{LR}}^{x_H=-2} \simeq \frac{(|q_{\text{SM}}^{e_L\mu_L}|^2 + |q_{\text{SM}}^{e_L\mu_R}|^2) - (|q_{\text{SM}}^{e_R\mu_R}|^2 + |q_{\text{SM}}^{e_R\mu_L}|^2)}{(|q_{\text{SM}}^{e_L\mu_L}|^2 + |q_{\text{SM}}^{e_L\mu_R}|^2) + (|q_{\text{SM}}^{e_R\mu_R}|^2 + |q_{\text{SM}}^{e_R\mu_L}|^2)}, \quad (50)$$

$$\mathcal{A}_{\text{LR}}^{x_H=-1} \simeq \frac{(|q_{\text{SM}}^{e_L\mu_L}|^2 + |q_{\text{SM}}^{e_L\mu_R}|^2) - (|q_{\text{SM}}^{e_R\mu_R}|^2 + |q_{\text{SM}}^{e_R\mu_L}|^2)}{(|q_{\text{SM}}^{e_L\mu_L}|^2 + |q_{\text{SM}}^{e_L\mu_R}|^2) + (|q_{\text{SM}}^{e_R\mu_R}|^2 + |q_{\text{SM}}^{e_R\mu_L}|^2)}. \quad (51)$$

In the case of the other x_H charges the BSM contributions come from all q^{XY} .

From Eq. (46) and Table IV we can write the integrated LR asymmetry for the $e^-e^+ \rightarrow b\bar{b}$ process at $x_H = -1$ and 1 as

$$\mathcal{A}_{\text{LR}}^{x_H=-1} \simeq \frac{(|q_{\text{SM}}^{e_L b_L}|^2 + |q_{\text{SM}}^{e_L b_R}|^2) - (|q_{\text{SM}}^{e_R b_R}|^2 + |q_{\text{SM}}^{e_R b_L}|^2)}{(|q_{\text{SM}}^{e_L b_L}|^2 + |q_{\text{SM}}^{e_L b_R}|^2) + (|q_{\text{SM}}^{e_R b_R}|^2 + |q_{\text{SM}}^{e_R b_L}|^2)}, \quad (52)$$

$$\mathcal{A}_{\text{LR}}^{x_H=1} \simeq \frac{(|q_{\text{SM}}^{e_L b_L}|^2 + |q_{\text{SM}}^{e_L b_R}|^2) - (|q_{\text{SM}}^{e_R b_R}|^2 + |q_{\text{SM}}^{e_R b_L}|^2)}{(|q_{\text{SM}}^{e_L b_L}|^2 + |q_{\text{SM}}^{e_L b_R}|^2) + (|q_{\text{SM}}^{e_R b_R}|^2 + |q_{\text{SM}}^{e_R b_L}|^2)}. \quad (53)$$

The BSM contributions are from the $|q^{XY}|$ quantities. For $x_H = 2$ the contribution will come from all $|q^{XY}|$. Similar behavior will be observed for the $t\bar{t}$ process where the BSM contributions will be associated with the choices of x_H following Table IV. From Fig. 13, we see that for all the fermion pair-production processes, the $x_H = -1$ case is

close to the SM, whereas other x_H charges can lead to significant differences with respect to the SM prediction.

The amount of deviation from the SM in the integrated LR asymmetry can be defined as

$$\Delta_{\mathcal{A}_{\text{LR}}} = \frac{\mathcal{A}_{\text{LR}}^{U(1)_X}}{\mathcal{A}_{\text{LR}}^{\text{SM}}} - 1, \quad (54)$$

respectively, which is shown in Fig. 14 as a function of the center-of-mass energy for the $\mu^+\mu^-$ (left), $b\bar{b}$ (middle), and $t\bar{t}$ (right) final states. The gray-shaded band shows the theoretically estimated statistical uncertainty [cf. Eq. (44)]. At $\sqrt{s} = 250$ GeV, the deviation in the $\mu^+\mu^-$ process can reach up to 1.5%, 3.1%, and 8.3% for $x_H = -2, 1, 2$, respectively, whereas that for $x_H = -1$ is below 1%. The deviations for the $\mu^+\mu^-$ process at 500 GeV can be 6.7%, 1.5%, 14%, and 38% for $x_H = -2, -1, 1$, and 2, respectively. The deviations increase up to 28%, 6.6%, 62%, and $>100\%$ for $x_H = -2, -1, 1$, and 2, respectively, at 1 TeV, and become very large at 3 TeV. Hence for the $\mu^+\mu^-$ final state $\Delta_{\mathcal{A}_{\text{LR}}}$ will be a very useful variable depending on the choice of x_H and \sqrt{s} .

The corresponding deviations for the $b\bar{b}$ process are much smaller: below 1% at 250 GeV for all x_H and within the theoretically estimated statistical error (similarly for the 500 GeV and 1 TeV colliders). The deviations will be roughly within 20%–40% at 3 TeV collider for all x_H except $x_H = -1$. As for the $t\bar{t}$ final state, the deviations can be 1.7%, 2.4%, and 6.5% for $x_H = -2, 1$, and 2,

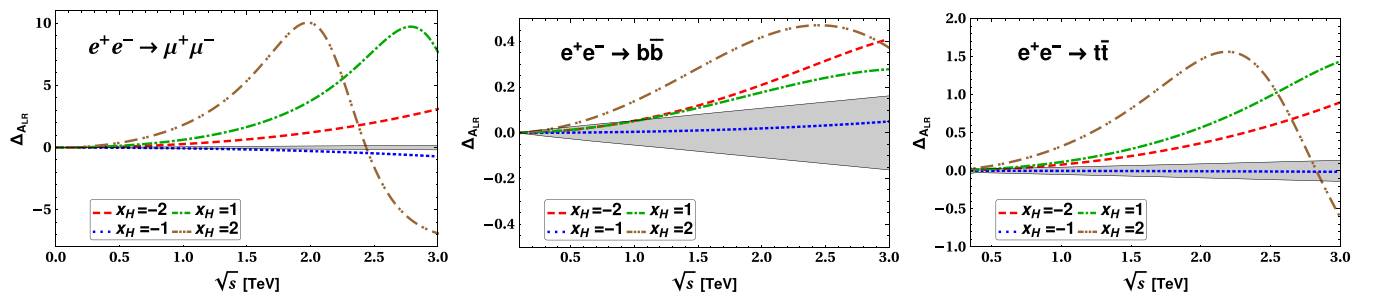


FIG. 14. The deviations in integrated LR asymmetry for the process $e^-e^+ \rightarrow f\bar{f}$ as a function of \sqrt{s} for $M_{Z'} = 7.5$ TeV. The contribution from theoretically estimated statistical deviations are shown by the gray shaded band.

respectively, at 500 GeV. At 1 TeV these values reach up to 8.1%, 11%, and 32% for $x_H = -2, 1, \text{ and } 2$, respectively. We find the deviation for $x_H = -1$ is throughout below 1%.

F. Left-right forward-backward asymmetry ($\mathcal{A}_{\text{LR,FB}}$)

The left-right forward-backward (LR, FB) asymmetry ($\mathcal{A}_{\text{LR,FB}}$) [63–66] can be defined as

$$\mathcal{A}_{\text{LR,FB}}(\cos\theta) = \frac{[\sigma_{\text{LR}}(\cos\theta) - \sigma_{\text{RL}}(\cos\theta)] - [\sigma_{\text{LR}}(-\cos\theta) - \sigma_{\text{RL}}(-\cos\theta)]}{[\sigma_{\text{LR}}(\cos\theta) + \sigma_{\text{RL}}(\cos\theta)] + [\sigma_{\text{LR}}(-\cos\theta) + \sigma_{\text{RL}}(-\cos\theta)]}. \quad (55)$$

In terms of the gauge interactions of the fermions, we write $\mathcal{A}_{\text{LR,FB}}$ as

$$\mathcal{A}_{\text{LR,FB}}(\cos\theta) = \frac{2\beta \cos\theta \{ (|q^{e_L f_L}|^2 + |q^{e_R f_L}|^2) - (|q^{e_L f_R}|^2 + |q^{e_R f_R}|^2) \}}{(1 + \beta^2 \cos^2\theta) \{ (|q^{e_L f_L}|^2 + |q^{e_R f_L}|^2) + (|q^{e_L f_R}|^2 + |q^{e_R f_R}|^2) \} + 8 \frac{m_f^2}{s} [\text{Re}(q^{e_L f_L} q^{e_L f_R*}) + \text{Re}(q^{e_R f_R} q^{e_R f_L*})]}. \quad (56)$$

For $m_f \ll \sqrt{s}$ the differential LR-FB asymmetry can be written as

$$\mathcal{A}_{\text{LR,FB}}(\cos\theta) \simeq \left[\frac{2 \cos\theta}{1 + \cos^2\theta} \right] \frac{(|q^{e_L f_L}|^2 + |q^{e_R f_L}|^2) - (|q^{e_L f_R}|^2 + |q^{e_R f_R}|^2)}{(|q^{e_L f_L}|^2 + |q^{e_R f_L}|^2) + (|q^{e_L f_R}|^2 + |q^{e_R f_R}|^2)}. \quad (57)$$

The observable LR-FB asymmetry can be written as

$$\mathcal{A}_{\text{LR,FB}}(P_{e^-}, P_{e^+}, \cos\theta) = \frac{[\sigma(P_{e^-}, P_{e^+}, \cos\theta) + \sigma(-P_{e^-}, -P_{e^+}, -\cos\theta)] - [\sigma(-P_{e^-}, -P_{e^+}, \cos\theta) + \sigma(P_{e^-}, P_{e^+}, -\cos\theta)]}{[\sigma(P_{e^-}, P_{e^+}, \cos\theta) + \sigma(-P_{e^-}, -P_{e^+}, -\cos\theta)] + [\sigma(-P_{e^-}, -P_{e^+}, \cos\theta) + \sigma(P_{e^-}, P_{e^+}, -\cos\theta)]}, \quad (58)$$

for $P_{e^-} < 0$ and $|P_{e^-}| > |P_{e^+}|$. The relation between $\mathcal{A}_{\text{LR,FB}}(\cos\theta)$ in Eq. (55) and $\mathcal{A}_{\text{LR,FB}}(P_{e^-}, P_{e^+}, \cos\theta)$ in Eq. (58) is given by

$$\mathcal{A}_{\text{LR,FB}}(\cos\theta) = \frac{1}{P_{\text{eff}}} \mathcal{A}_{\text{LR,FB}}(P_{e^-}, P_{e^+}, \cos\theta). \quad (59)$$

The differential LR-FB asymmetry defined in Eq. (57) as a function of $\cos\theta$ for $M_{Z'} = 7.5$ TeV is shown in Fig. 15 for $\mu^- \mu^+$ (top panel), $b\bar{b}$ (middle panel), and $t\bar{t}$ (bottom panel). We consider four different x_H values and compare with the SM case (solid black line) in each case at $\sqrt{s} = 250$ GeV (except $t\bar{t}$), 500 GeV, 1 TeV, and 3 TeV. The shift

from the SM becomes prominent with the increase in \sqrt{s} . For the $e^- e^+ \rightarrow \mu^- \mu^+$ process, it starts to become noticeable from $\sqrt{s} = 250$ GeV depending on x_H and $\cos\theta$. The differential LR-FB asymmetry for $b\bar{b}$ process also follows the same behavior from $\sqrt{s} = 1$ TeV. For $t\bar{t}$ process the asymmetry parameter starts to become different from the SM results from $\sqrt{s} = 500$ GeV depending on x_H and $\cos\theta$. The LR-FB asymmetry involves the couplings of the Z' with the SM charged fermions which contain BSM effects governed by Table IV.

From Eqs. (56), (57) and using Table IV the differential LR-FB asymmetry for the $e^- e^+ \rightarrow \mu^- \mu^+$ process for $x_H = -2$ and -1 can be written as

$$\mathcal{A}_{\text{LR,FB}}(\cos\theta)^{x_H=-2} \simeq \left[\frac{2 \cos\theta}{1 + \cos^2\theta} \right] \frac{(|q_{\text{SM}}^{e_L \mu_L}|^2 + |q_{\text{SM}}^{e_R \mu_L}|^2) - (|q_{\text{SM}}^{e_L \mu_R}|^2 + |q_{\text{SM}}^{e_R \mu_R}|^2)}{(|q_{\text{SM}}^{e_L \mu_L}|^2 + |q_{\text{SM}}^{e_R \mu_L}|^2) + (|q_{\text{SM}}^{e_L \mu_R}|^2 + |q_{\text{SM}}^{e_R \mu_R}|^2)}, \quad (60)$$

$$\mathcal{A}_{\text{LR,FB}}(\cos\theta)^{x_H=-1} \simeq \left[\frac{2 \cos\theta}{1 + \cos^2\theta} \right] \frac{(|q_{\text{SM}}^{e_L \mu_L}|^2 + |q_{\text{SM}}^{e_R \mu_L}|^2) - (|q_{\text{SM}}^{e_L \mu_R}|^2 + |q_{\text{SM}}^{e_R \mu_R}|^2)}{(|q_{\text{SM}}^{e_L \mu_L}|^2 + |q_{\text{SM}}^{e_R \mu_L}|^2) + (|q_{\text{SM}}^{e_L \mu_R}|^2 + |q_{\text{SM}}^{e_R \mu_R}|^2)}. \quad (61)$$

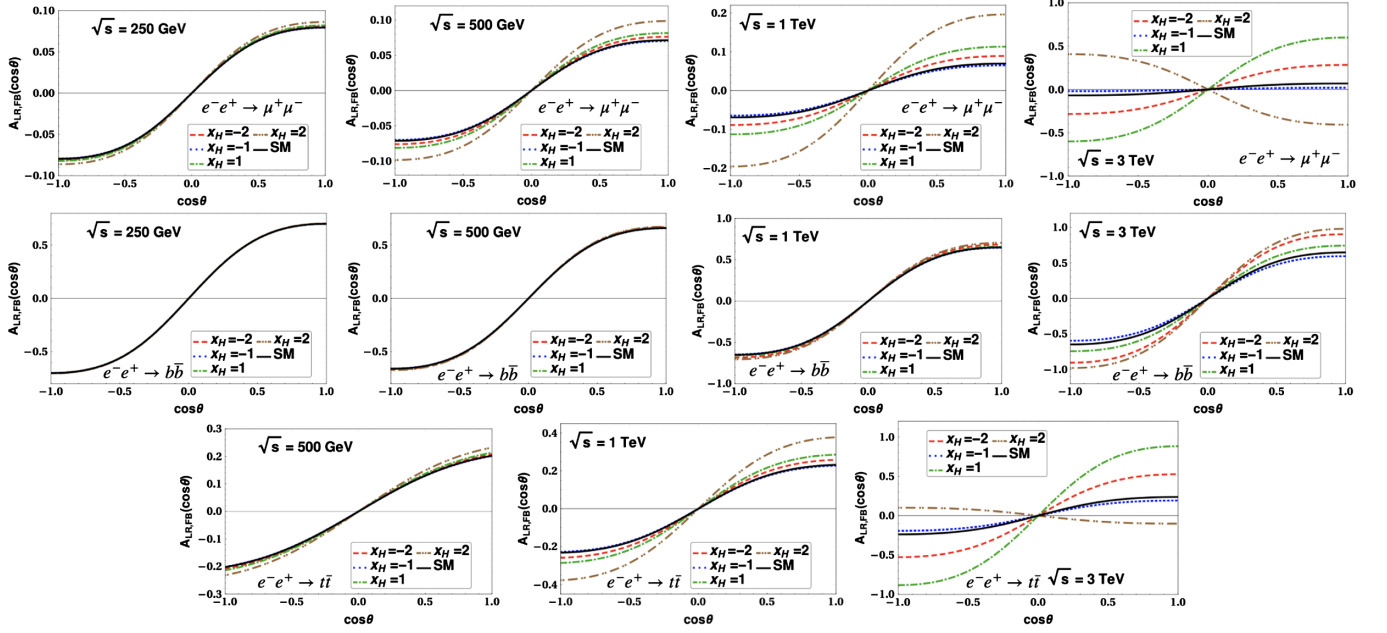


FIG. 15. The differential LR-FB asymmetry for the $e^-e^+ \rightarrow f\bar{f}$ process as a function of $\cos\theta$ considering $M_{Z'} = 7.5$ TeV. The SM result is shown by the black solid line.

In the case of the $e^-e^+ \rightarrow b\bar{b}$ process, the differential LR-FB asymmetries for $x_H = -1$ and 1 can be written as

$$A_{\text{LR,FB}}(\cos\theta)^{x_H=-1} \simeq \left[\frac{2 \cos\theta}{1 + \cos^2\theta} \right] \frac{(|q^{e_L b_L}|^2 + |q_{\text{SM}}^{e_R b_L}|^2) - (|q^{e_L b_R}|^2 + |q_{\text{SM}}^{e_R b_R}|^2)}{(|q^{e_L b_L}|^2 + |q_{\text{SM}}^{e_R b_L}|^2) + (|q^{e_L b_R}|^2 + |q_{\text{SM}}^{e_R b_R}|^2)}, \quad (62)$$

$$A_{\text{LR,FB}}(\cos\theta)^{x_H=1} \simeq \left[\frac{2 \cos\theta}{1 + \cos^2\theta} \right] \frac{(|q^{e_L b_L}|^2 + |q^{e_R b_L}|^2) - (|q_{\text{SM}}^{e_L b_R}|^2 + |q_{\text{SM}}^{e_R b_R}|^2)}{(|q^{e_L b_L}|^2 + |q^{e_R b_L}|^2) + (|q_{\text{SM}}^{e_L b_R}|^2 + |q_{\text{SM}}^{e_R b_R}|^2)}. \quad (63)$$

For $x_H = 2$ all q^{XY} contribute in the differential LR-FB asymmetry in the $b\bar{b}$ process. Similar behavior is observed in case of $e^-e^+ \rightarrow t\bar{t}$ process depending on the choices of x_H and following Table IV. The nature of the differential LR-FB asymmetry is governed by the term $\frac{\cos\theta}{1+\cos^2\theta}$. In the case of the $\mu^+\mu^-$ process the BSM effect is nominal for $x_H = 1$ and 2 at $\sqrt{s} = 250$ GeV for larger values of $|\cos\theta|$; however, with the increase in \sqrt{s} the differential LR-FB asymmetry becomes prominently different from the SM results. Similar behavior can be observed for the $b\bar{b}$ and $t\bar{t}$ processes depending on \sqrt{s} and θ .

The deviation in the differential LR-FB asymmetry from the SM can be defined as

$$\Delta_{\text{LR,FB}} = \frac{A_{\text{LR,FB}}^{U(1)_X}(\cos\theta)}{A_{\text{LR,FB}}^{\text{SM}}(\cos\theta)} - 1. \quad (64)$$

This is shown as a function of $\cos\theta$ in Fig. 16 for $\mu^+\mu^-$ (top panel), $b\bar{b}$ (middle panel), and $t\bar{t}$ (bottom panel) taking $M_{Z'} = 7.5$ TeV and x_H as $-2, -1, 1, 2$. The gray-shaded region in each figure represents the theoretically estimated statistical error, given by

$$\Delta_{\text{LR,FB}}^{\text{stat}} = 2 \frac{(n_3 + n_2)(\sqrt{n_1} + \sqrt{n_4}) + (n_1 + n_4)(\sqrt{n_3} + \sqrt{n_2})}{(n_1 + n_4)^2 - (n_3 + n_2)^2} A_{\text{LR,FB}}, \quad (65)$$

where $(n_1, n_2, n_3, n_4) = (N_{\text{LRF}}, N_{\text{RLF}}, N_{\text{LRB}}, N_{\text{RLB}})$, $N_{iF} = \mathcal{L}_{\text{int}}\sigma_i([0, \cos\theta])$ and $N_{iB} = \mathcal{L}_{\text{int}}\sigma_i([- \cos\theta, 0])$ with $(i = \text{LR}, \text{RL})$. $\Delta_{\text{LR,FB}}$ is a ratio between the two differential LR-FB quantities. As a result the model independent

quantity $\frac{\cos\theta}{1+\cos^2\theta}$ gets canceled from the numerator and denominator. Therefore the deviations in the differential LR-FB asymmetry are independent of $\cos\theta$. The variation with respect to x_H involves the BSM effects from different

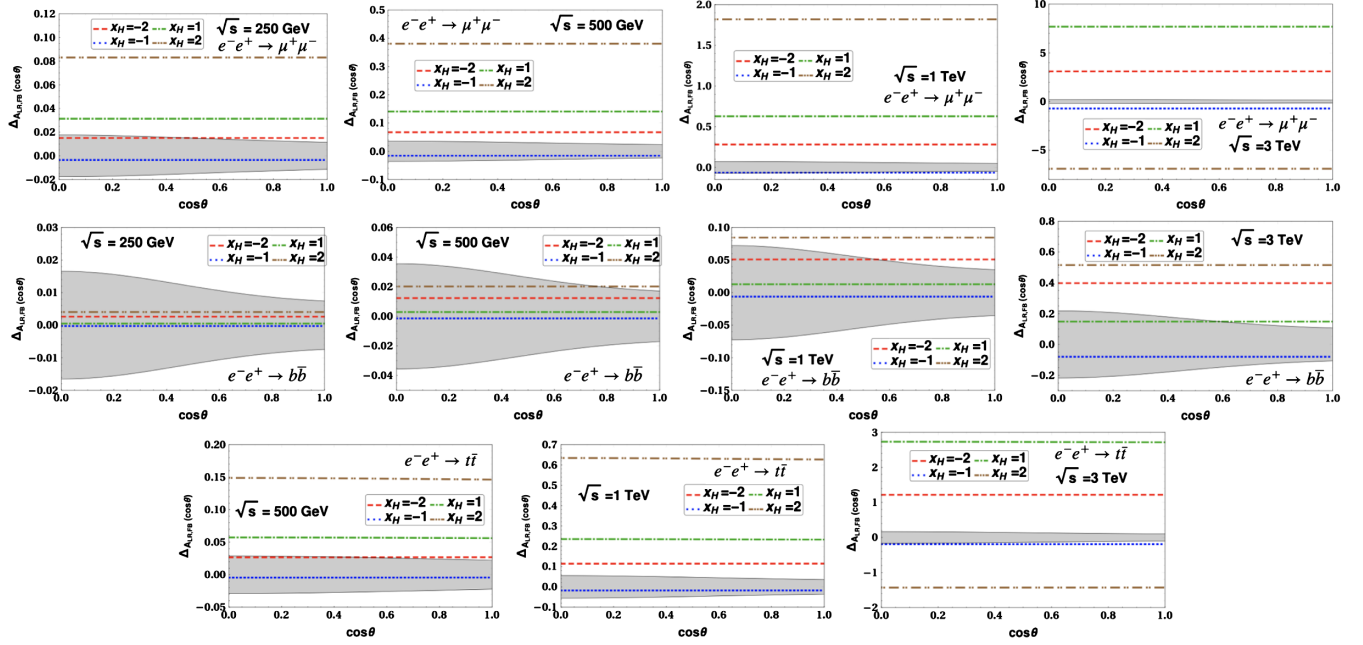


FIG. 16. The deviation in the differential LR-FB asymmetry for the $e^-e^+ \rightarrow f\bar{f}$ process as a function of $\cos\theta$ considering $M_{Z'} = 7.5 \text{ TeV}$. The theoretically estimated statistical error is shown by the gray-shaded region. The integrated luminosity $\mathcal{L}_{\text{int}} = 1 \text{ ab}^{-1}$.

q^{XY} following Table IV. We also comment from Fig. 15 that $A_{\text{LR,FB}}(\cos\theta)$ is an antisymmetric function of $\cos\theta$, hence the integrated $A_{\text{LR,FB}}$ will be zero. Therefore for the LR-FB asymmetry, only the differential variables are useful to study.

From Fig. 16 we obtain that $\mu^-\mu^+$ process can have a sizable deviation around 3.2% and 8.4% for $x_H = 1$ and 2 at $\sqrt{s} = 250 \text{ GeV}$, respectively, from the SM. At $\sqrt{s} = 500 \text{ GeV}$ the deviation increases up to 6.2%, 14%, and 38% from $x_H = -2, 1,$ and 2, respectively. The corresponding deviations become orders of magnitude higher at $\sqrt{s} = 1$ and 3 TeV, respectively. We notice similar behavior for the $b\bar{b}$ and $t\bar{t}$ processes, however, the deviations depend on \sqrt{s} and x_H . We have noticed that the deviation is negative in some cases where the observable quantity is subdominant over the SM case.

IV. OBSERVABLES FOR THE BHABHA SCATTERING PROCESS

For $f = e$ in the process $e^-e^+ \rightarrow f\bar{f}$, we get the Bhabha scattering which has both s -channel and t -channel contributions from neutral vector bosons. In the SM, the Bhabha scattering is induced by γ and Z -mediated channels, whereas in the $U(1)_X$ model an additional contribution from the Z' boson is present. These three channels also interfere due to presence same initial and final states. The coupling between Z' and the electron contains the $U(1)_X$ charge. As a result the effect of x_H will be manifest in the Bhabha scattering.

For the longitudinally polarized initial states the differential scattering cross section can be written as

$$\begin{aligned} \frac{d\sigma}{d\cos\theta}(P_{e^-}, P_{e^+}) = & \frac{1}{4} \left\{ (1 - P_{e^-})(1 - P_{e^+}) \frac{d\sigma_{e_L^- e_L^+}}{d\cos\theta} \right. \\ & + (1 + P_{e^-})(1 + P_{e^+}) \frac{d\sigma_{e_R^- e_R^+}}{d\cos\theta} \\ & + (1 - P_{e^-})(1 + P_{e^+}) \frac{d\sigma_{e_L^- e_R^+}}{d\cos\theta} \\ & \left. + (1 + P_{e^-})(1 - P_{e^+}) \frac{d\sigma_{e_R^- e_L^+}}{d\cos\theta} \right\}. \end{aligned} \quad (66)$$

The corresponding differential scattering cross sections can be written as

$$\frac{d\sigma_{e_L^- e_L^+}}{d\cos\theta} = \frac{1}{8\pi s} [u^2 |q_s(s)^{\text{LL}} + q_t(s, \theta)^{\text{LL}}|^2 + t^2 |q_s(s)^{\text{LR}}|^2], \quad (67)$$

$$\frac{d\sigma_{e_R^- e_R^+}}{d\cos\theta} = \frac{1}{8\pi s} [u^2 |q_s(s)^{\text{RR}} + q_t(s, \theta)^{\text{RR}}|^2 + t^2 |q_s(s)^{\text{LR}}|^2], \quad (68)$$

$$\begin{aligned} \frac{d\sigma_{e_L^- e_L^+}}{d\cos\theta} &= \frac{1}{8\pi s} [s^2 |q_t(s, \theta)^{\text{LR}}|^2], \\ \frac{d\sigma_{e_R^- e_R^+}}{d\cos\theta} &= \frac{1}{8\pi s} [s^2 |q_t(s, \theta)^{\text{LR}}|^2], \end{aligned} \quad (69)$$

where s , t , and u are the Mandelstam variables given by $s = (E_{e^-} + E_{e^+})^2$, $t = -s \sin^2 \frac{\theta}{2}$, and $u = -s \cos^2 \frac{\theta}{2}$, and E_{e^+} , E_{e^-} are the incoming electron and positron energies, respectively. The quantities $q_{s(t)}$ are the corresponding s (t)-channel propagators. The propagators for the s -channel process can be written as

$$q_s(s)^{\text{LL}} = \frac{e^2}{s} + \frac{g_L^2}{s - M_Z^2 + iM_Z\Gamma_Z} + \frac{g'_L{}^2}{s - M_{Z'}^2 + iM_{Z'}\Gamma_{Z'}}, \quad (70)$$

$$q_s(s)^{\text{RR}} = \frac{e^2}{s} + \frac{g_R^2}{s - M_Z^2 + iM_Z\Gamma_Z} + \frac{g'_R{}^2}{s - M_{Z'}^2 + iM_{Z'}\Gamma_{Z'}}, \quad (71)$$

$$\begin{aligned} q_s(s)^{\text{LR}} &= q_s(s)^{\text{RL}} \\ &= \frac{e^2}{s} + \frac{g_L g_R}{s - M_Z^2 + iM_Z\Gamma_Z} + \frac{g'_L g'_R}{s - M_{Z'}^2 + iM_{Z'}\Gamma_{Z'}}, \end{aligned} \quad (72)$$

and those for the t -channel process are

$$q_t(s, \theta)^{\text{LL}} = \frac{e^2}{t} + \frac{g_L^2}{t - M_Z^2 + iM_Z\Gamma_Z} + \frac{g'_L{}^2}{t - M_{Z'}^2 + iM_{Z'}\Gamma_{Z'}}, \quad (73)$$

$$q_t(s, \theta)^{\text{RR}} = \frac{e^2}{t} + \frac{g_R^2}{t - M_Z^2 + iM_Z\Gamma_Z} + \frac{g'_R{}^2}{t - M_{Z'}^2 + iM_{Z'}\Gamma_{Z'}}, \quad (74)$$

$$\begin{aligned} q_t(s, \theta)^{\text{LR}} &= q_t(s, \theta)^{\text{RL}} \\ &= \frac{e^2}{t} + \frac{g_L g_R}{t - M_Z^2 + iM_Z\Gamma_Z} + \frac{g'_L g'_R}{t - M_{Z'}^2 + iM_{Z'}\Gamma_{Z'}}. \end{aligned} \quad (75)$$

Here $e = \sqrt{4\pi\alpha}$, $\alpha = \frac{1}{137}$, g_L , g_R are the left- and right-handed couplings of the electron with the Z boson, and g'_L , g'_R are the left- and right-handed couplings of the electron with the Z' boson, respectively. Using the above expressions, we define

$$\begin{aligned} s|q^{\text{LL}}| &= s|q_s(s)^{\text{LL}} + q_t(s, \theta)^{\text{LL}}|, \\ s|q^{\text{LR}}| &= s|q_s(s)^{\text{LR}} + q_t(s, \theta)^{\text{LR}}|, \\ s|q^{\text{RL}}| &= s|q_s(s)^{\text{RL}} + q_t(s, \theta)^{\text{RL}}|, \\ s|q^{\text{RR}}| &= s|q_s(s)^{\text{RR}} + q_t(s, \theta)^{\text{RR}}|, \end{aligned} \quad (76)$$

which are plotted in Fig. 17 for the SM (top left) and also for the $U(1)_X$ model with different x_H values. We have fixed $M_{Z'} = 7.5$ TeV and $g' = 0.4$. For the t -channel propagator we consider $\cos \theta = 0.5$. For $x_H = -2$ here is no coupling between ℓ_L and Z' and for $x_H = -1$ there is no coupling between e_R and Z' .

A. Differential and integrated cross sections

The differential scattering cross section from Eq. (66) can be written as

$$\frac{d\sigma}{d\cos\theta} = \frac{d\sigma^s}{d\cos\theta} + \frac{d\sigma^t}{d\cos\theta} + \frac{d\sigma^{st}}{d\cos\theta}, \quad (77)$$

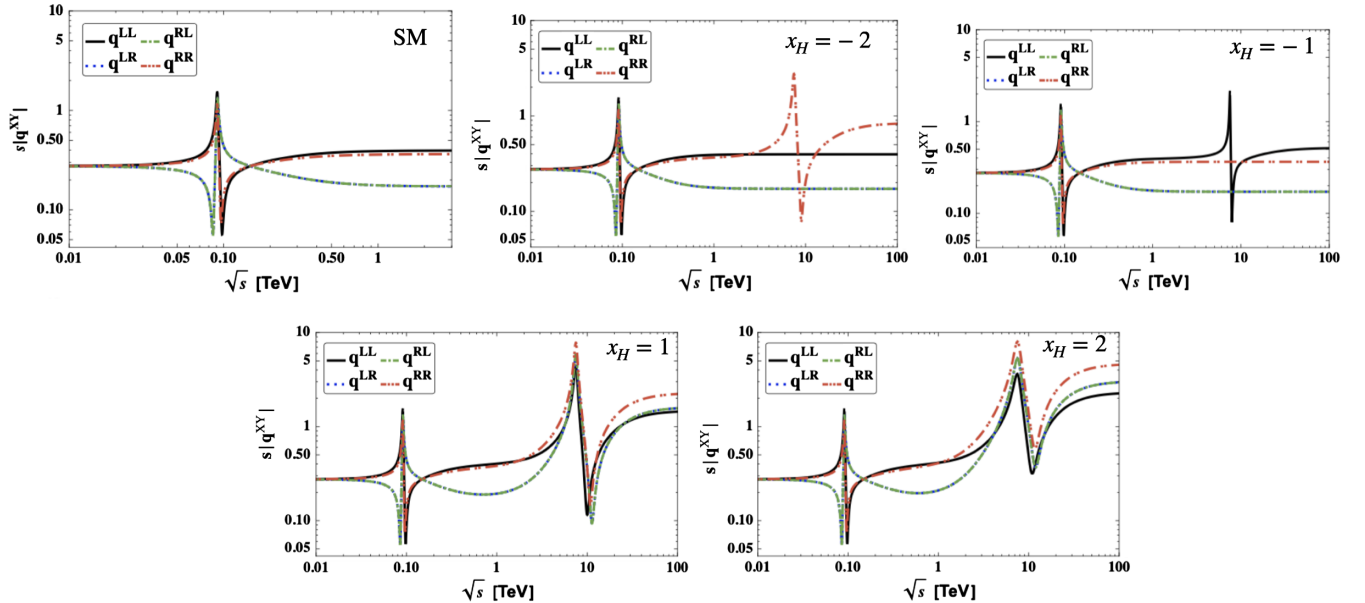


FIG. 17. $s|q^{XY}|$ as a function of \sqrt{s} for the Bhabha scattering considering $M_{Z'} = 7.5$ TeV and $g' = 0.4$.

where the three terms correspond to the s -channel, t -channel, and interference between them, respectively. Explicitly,

$$\begin{aligned} \frac{d\sigma^s}{d\cos\theta} &= \frac{1}{32\pi s} [(1 + P_{e^-})(1 - P_{e^+}) \\ &\quad \times \{u^2 |q_s(s)^{\text{RR}}|^2 + t^2 |q_s(s)^{\text{LR}}|^2\} \\ &\quad + (1 - P_{e^-})(1 + P_{e^+}) \\ &\quad \times \{u^2 |q_s(s)^{\text{LL}}|^2 + t^2 |q_s(s)^{\text{LR}}|^2\}], \end{aligned} \quad (78)$$

$$\begin{aligned} \frac{d\sigma^t}{d\cos\theta} &= \frac{1}{32\pi s} [(1 - P_{e^-})(1 + P_{e^+})u^2 |q_t(s, \theta)^{\text{LL}}|^2 \\ &\quad + (1 + P_{e^-})(1 - P_{e^+})u^2 |q_t(s, \theta)^{\text{RR}}|^2 \\ &\quad + (1 - P_{e^-})(1 - P_{e^+})s^2 |q_t(s, \theta)^{\text{LR}}|^2 \\ &\quad + (1 + P_{e^-})(1 + P_{e^+})s^2 |q_t(s, \theta)^{\text{LR}}|^2], \end{aligned} \quad (79)$$

$$\begin{aligned} \frac{d\sigma^{st}}{d\cos\theta} &= \frac{1}{16\pi s} u^2 [(1 - P_{e^-})(1 + P_{e^+})\text{Re}(q_s(s)^{\text{LL}} q_t^*(s, \theta)^{\text{LL}}) \\ &\quad + (1 + P_{e^-})(1 - P_{e^+})\text{Re}(q_s(s)^{\text{RR}} q_t^*(s, \theta)^{\text{RR}})]. \end{aligned} \quad (80)$$

The deviation from the SM for the differential and integrated scattering cross sections can, respectively, be written as

$$\begin{aligned} \Delta_{d\sigma}(P_{e^-}, P_{e^+}, \cos\theta) &= \frac{d\sigma^{U(1)_X}}{d\cos\theta} - \frac{d\sigma^{\text{SM}}}{d\cos\theta}, \\ \Delta_{\sigma}(P_{e^-}, P_{e^+}) &= \frac{\sigma^{U(1)_X}}{\sigma^{\text{SM}}} - 1. \end{aligned} \quad (81)$$

The estimated statistical error can theoretically be calculated as

$$\Delta\sigma(P_{e^-}, P_{e^+}, -\cos\theta_{\min}, +\cos\theta_{\max}) = \frac{\sigma}{\sqrt{\mathcal{L}_{\text{int}}\sigma}}. \quad (82)$$

The total production cross sections of the $e^-e^+ \rightarrow e^-e^+$ process for three choices of the polarization states and different x_H with $M_{Z'} = 7.5$ TeV have been shown in the upper part of Fig. 18. In this analysis we consider $g' = 0.4$. The corresponding deviations from the SM production process are shown in the lower part of the same figure. The SM result is represented by the black solid line. The $U(1)_X$ case has been studied for $x_H = -2, -1, 1, \text{ and } 2$. The result depends on the choices of $M_{Z'}$, \sqrt{s} , and g' . Larger values of g' can widen the width of the resonance. Depending on the polarization of the initial states and x_H , the deviation in the total cross section reaches up to a very large margin with the increase in \sqrt{s} , say at $\sqrt{s} = 3$ TeV. The deviations between the SM and the $U(1)_X$ cross sections depend on the Z' -mediated processes and its interference with γ and Z -mediated processes. In our model setup for $x_H = -2$ there is no coupling between Z' and ℓ_L and for $x_H = -1$ there is no coupling between Z' and e_R . The effect of the vanishing couplings are manifest in the production cross sections and the corresponding deviations. The effects for $x_H = 1$ and 2 are different where both the left- and right-handed electrons have nonvanishing couplings with Z' . The largest deviation in the total cross section can reach up to 100% or more for larger \sqrt{s} depending on x_H and g' .

The deviations in the total cross sections from the SM for different x_H can be obtained from Eq. (81). Fixing \sqrt{s} the deviations as a function of the electron polarization (P_{e^-}) are shown in Fig. 19 for $M_{Z'} = 7.5$ TeV. We set positron polarization (P_{e^+}) at zero for this analysis. We show the deviations for $\sqrt{s} = 250$ GeV, 500 GeV, 1 TeV, and 3 TeV. The deviation for $x_H = -1$ decreases with the increase in P_{e^-} as the coupling of e_R with Z' vanishes, whereas for the other choices the deviation increases with the increase in P_{e^-} . The maximum deviation can be attained for $x_H = 2$ for all the values of \sqrt{s} . At $\sqrt{s} = 250$ GeV, the deviation can reach up to 0.55% whereas that can be nearly 2.5% at $\sqrt{s} = 500$ GeV, 10% at $\sqrt{s} = 1$ TeV and more than 100% at $\sqrt{s} = 3$ TeV depending on the choice of P_{e^-} . The

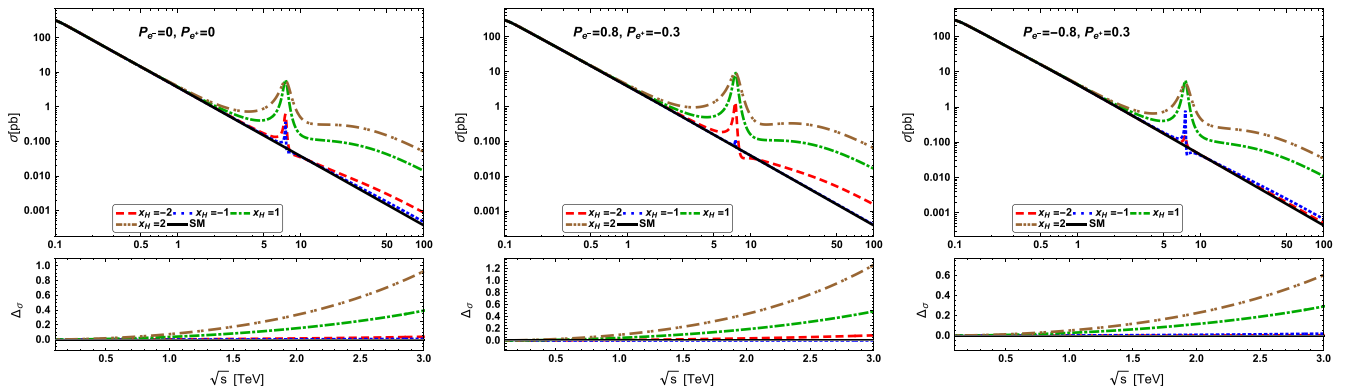


FIG. 18. Total scattering cross sections for the Bhabha scattering (upper part of each panel) and the corresponding deviations from the SM (lower part of each panel) as a function of \sqrt{s} for $M_{Z'} = 7.5$ TeV and $g' = 0.4$.

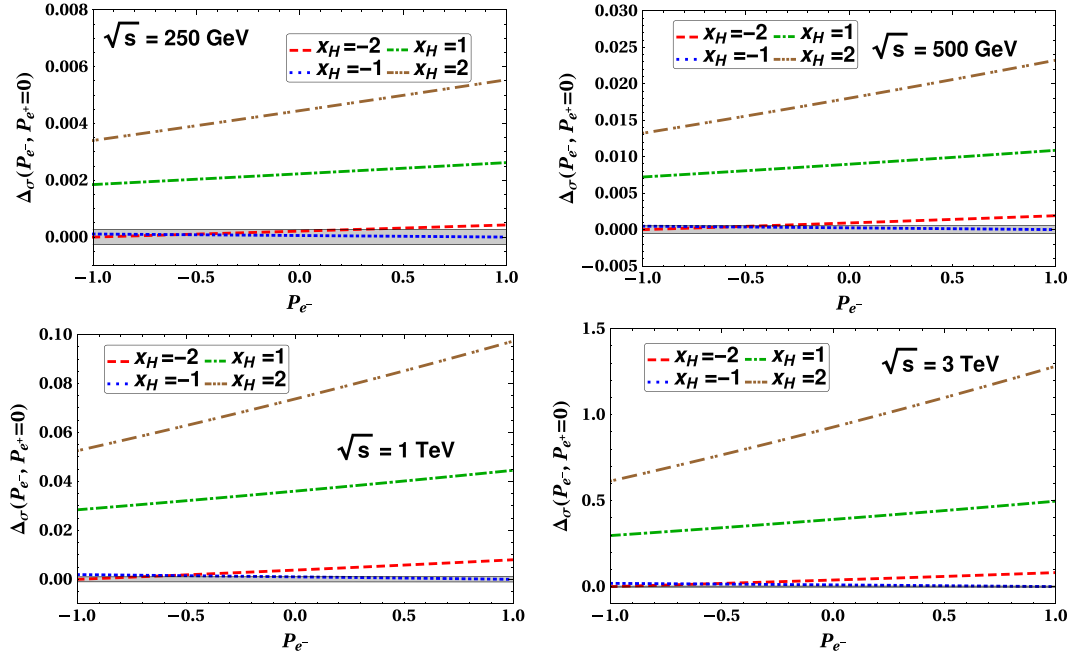


FIG. 19. The deviations of the total cross section as a function of electron polarization (P_{e^-}) for $M_{Z'}$ = 7.5 TeV and $g' = 0.4$ setting $P_{e^+} = 0$ for different \sqrt{s} . The gray band shows the theoretically estimated statistical error.

theoretically estimated statistical error from Eq. (82) is shown by the gray band which becomes narrower with \sqrt{s} , as it is inversely proportional to $\sqrt{\sigma}$.

B. Differential and integrated LR asymmetries

The $e^-e^+ \rightarrow e^-e^+$ process contains t -channel scattering; hence the forward scattering dominates. Therefore the FB

asymmetry \mathcal{A}_{FB} is not a well-measured quantity for Bhabha scattering. On the other hand, the LR asymmetry can be measured when the initial electron and/or positron is longitudinally polarized.

The LR asymmetry of the differential cross section for $1 \geq P_- \geq 0$ and $1 \geq P_+ \geq -1$ can be written as

$$\begin{aligned}
 \mathcal{A}_{\text{LR}}(P_-, P_+, \cos\theta) &= \frac{\frac{d\sigma}{d\cos\theta}(P_{e^-} = -P_-, P_{e^+} = -P_+) - \frac{d\sigma}{d\cos\theta}(P_{e^-} = +P_-, P_{e^+} = +P_+)}{\frac{d\sigma}{d\cos\theta}(P_{e^-} = -P_-, P_{e^+} = -P_+) + \frac{d\sigma}{d\cos\theta}(P_{e^-} = +P_-, P_{e^+} = +P_+)} \\
 &= \frac{(P_- - P_+) \left(\frac{d\sigma_{e_L^- e_R^+}}{d\cos\theta} - \frac{d\sigma_{e_R^- e_L^+}}{d\cos\theta} \right)}{(1 + P_- P_+) \left(\frac{d\sigma_{e_L^- e_L^+}}{d\cos\theta} + \frac{d\sigma_{e_R^- e_R^+}}{d\cos\theta} \right) + (1 - P_- P_+) \left(\frac{d\sigma_{e_L^- e_R^+}}{d\cos\theta} + \frac{d\sigma_{e_R^- e_L^+}}{d\cos\theta} \right)} \\
 &= \frac{(P_- - P_+) \left\{ u^2 (|q_s(s)^{\text{LL}} + q_t(s, \theta)^{\text{LL}}|^2 - |q_s(s)^{\text{RR}} + q_t(s, \theta)^{\text{RR}}|^2) \right\}}{(1 + P_- P_+) (2s^2 |q_t(s, \cos\theta)^{\text{LR}}|^2) + (1 - P_- P_+) \left\{ u^2 (|q_s(s)^{\text{LL}} + q_t(s, \theta)^{\text{LL}}|^2 + |q_s(s)^{\text{RR}} + q_t(s, \theta)^{\text{RR}}|^2) + 2t^2 |q_s(s)^{\text{LR}}|^2 \right\}}.
 \end{aligned} \tag{83}$$

The LR asymmetry will vanish if both the initial states are unpolarized.

The integrated LR asymmetry of the polarized cross sections can be given as

$$\begin{aligned}
\mathcal{A}_{LR}(P_-, P_+) &= \frac{\sigma(P_{e^-} = -P_-, P_{e^+} = -P_+) - \sigma(P_{e^-} = +P_-, P_{e^+} = +P_+)}{\sigma(P_{e^-} = -P_-, P_{e^+} = -P_+) + \sigma(P_{e^-} = +P_-, P_{e^+} = +P_+)} \\
&= \frac{(P_- + P_+)(\sigma_{e_L^- e_L^+} - \sigma_{e_R^- e_R^+}) + (P_- - P_+)(\sigma_{e_L^- e_R^+} - \sigma_{e_R^- e_L^+})}{(1 + P_- P_+)(\sigma_{e_L^- e_L^+} + \sigma_{e_R^- e_R^+}) + (1 - P_- P_+)(\sigma_{e_L^- e_R^+} + \sigma_{e_R^- e_L^+})} \\
&= (P_- - P_+) \frac{\sigma_{e_L^- e_R^+} - \sigma_{e_R^- e_L^+}}{(1 + P_- P_+)(\sigma_{e_L^- e_L^+} + \sigma_{e_R^- e_R^+}) + (1 - P_- P_+)(\sigma_{e_L^- e_R^+} + \sigma_{e_R^- e_L^+})}, \tag{84}
\end{aligned}$$

where the quantity σ can be obtained by integrating over the scattering angle θ as

$$\sigma = \int_{\cos\theta_{\min}}^{\cos\theta_{\max}} \frac{d\sigma}{d\cos\theta} d\cos\theta. \tag{85}$$

Due to $\frac{d\sigma_{e_L^- e_L^+}}{d\cos\theta} = \frac{d\sigma_{e_R^- e_R^+}}{d\cos\theta}$ we get $\sigma_{e_L^- e_L^+} = \sigma_{e_R^- e_R^+}$.

The deviation from the SM in the differential and integrated LR asymmetries can be written as

$$\Delta_{\mathcal{A}_{LR}}(\cos\theta) = \frac{\mathcal{A}_{LR}^{U(1)_X}(\cos\theta)}{\mathcal{A}_{LR}^{\text{SM}}(\cos\theta)} - 1, \quad \Delta_{\mathcal{A}_{LR}} = \frac{\mathcal{A}_{LR}^{U(1)_X}}{\mathcal{A}_{LR}^{\text{SM}}} - 1, \tag{86}$$

respectively. The theoretically estimated statistical error can be estimated as

$$\Delta_{\mathcal{A}_{LR}} = \frac{2\sqrt{N_1 N_2}}{(N_1 + N_2)(\sqrt{N_1} - \sqrt{N_2})} \mathcal{A}_{LR}, \tag{87}$$

where $N_1 = \mathcal{L}_{\text{int}}\sigma(P_{e^-} = -P_-, P_{e^+} = -P_+)$ and $N_2 = \mathcal{L}_{\text{int}}\sigma(P_{e^-} = +P_-, P_{e^+} = +P_+)$.

The differential LR asymmetry from Eq. (83) is shown with two sets of polarizations $(P_-, P_+) = (0.8, 0.3)$ and $(0.8, -0.3)$ in the upper and lower panels of Fig. 20, respectively, for $M_{Z'} = 7.5$ TeV. We consider $\sqrt{s} = 250$ GeV, 500 GeV, 1 TeV, and 3 TeV for different x_H from left to right in each panel. Theoretically estimated statistical error is shown by the gray band using Eq. (87) which becomes narrower with the increase in the scattering angle and \sqrt{s} . The SM result is shown by the solid black line. For $x_H = -2$ there is no interaction between e_L and Z' and for $x_H = -1$ there is no interaction between e_R and Z' . These properties will affect the LR asymmetry. In the case of $x_H = -2$ the BSM contribution comes from q^{RR} only and for $x_H = -1$ the BSM contribution comes from q^{LL} only. For the other two choices of x_H the BSM contributions come from all q^{XY} . From Eq. (83) the differential LR asymmetry for $x_H = -2$ and -1 can be written as

$$\begin{aligned}
&\mathcal{A}_{LR}(P_-, P_+, \cos\theta)^{x_H=-2} \\
&= \frac{(P_- - P_+) \{u^2(|q_s(s)_{\text{SM}}^{\text{LL}} + q_t(s, \theta)_{\text{SM}}^{\text{LL}}|^2 - |q_s(s)^{\text{RR}} + q_t(s, \theta)^{\text{RR}}|^2)\}}{(1 + P_- P_+) (2s^2 |q_t(s, \cos\theta)_{\text{SM}}^{\text{LR}}|^2) + (1 - P_- P_+) \{u^2(|q_s(s)_{\text{SM}}^{\text{LL}} + q_t(s, \theta)_{\text{SM}}^{\text{LL}}|^2 + |q_s(s)^{\text{RR}} + q_t(s, \theta)^{\text{RR}}|^2) + 2t^2 |q_s(s)_{\text{SM}}^{\text{LR}}|^2\}}, \tag{88}
\end{aligned}$$

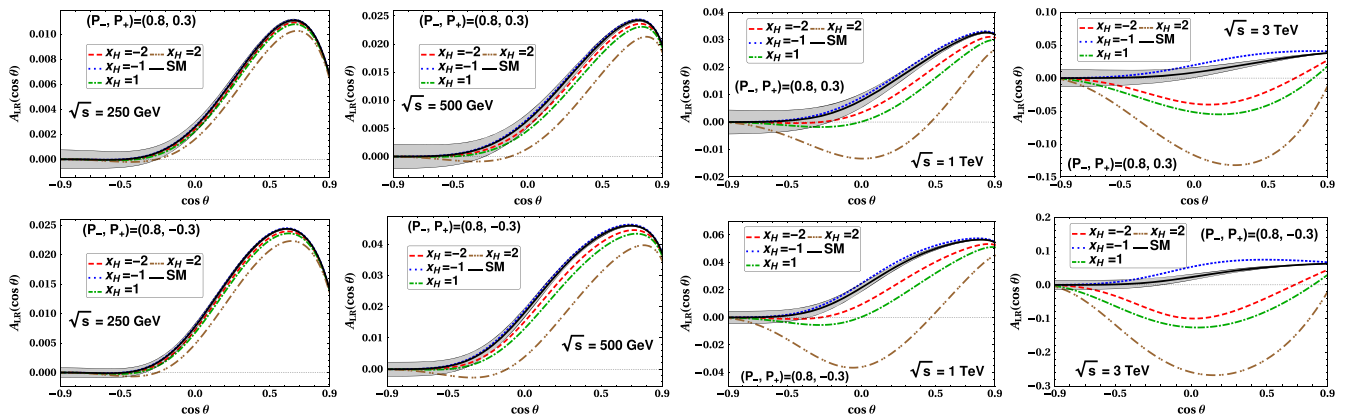


FIG. 20. Polarized differential LR asymmetry as a function of $\cos\theta$ for fixed \sqrt{s} taking different values of x_H considering $M_{Z'} = 7.5$ TeV and $g' = 0.4$. The SM result is shown by the black solid line. The theoretically estimated statistical error is represented by the gray-shaded region.

$$\begin{aligned}
 & \mathcal{A}_{\text{LR}}(P_-, P_+, \cos\theta)^{x_H=-1} \\
 &= \frac{(P_- - P_+) \left\{ u^2 (|q_s(s)^{\text{LL}} + q_t(s, \theta)^{\text{LL}}|^2 - |q_s(s)^{\text{RR}}_{\text{SM}} + q_t(s, \theta)^{\text{RR}}_{\text{SM}}|^2) \right\}}{(1 + P_- P_+) (2s^2 |q_t(s, \cos\theta)^{\text{LR}}_{\text{SM}}|^2) + (1 - P_- P_+) \left\{ u^2 (|q_s(s)^{\text{LL}} + q_t(s, \theta)^{\text{LL}}|^2 + |q_s(s)^{\text{RR}}_{\text{SM}} + q_t(s, \theta)^{\text{RR}}_{\text{SM}}|^2) + 2t^2 |q_s(s)^{\text{LR}}_{\text{SM}}|^2 \right\}}.
 \end{aligned} \tag{89}$$

The asymmetries are beyond the range of the theoretically estimated statistical error for $\cos\theta > 0$ and $x_H = 2$ for both sets of polarizations at $\sqrt{s} = 250$ GeV. The results for $x_H = -2$ and 1 are also outside the range of the

statistical error; however, the difference is not large. The deviations in the asymmetry from the SM result become more prominent for larger \sqrt{s} for both $\cos\theta < 0$ and $\cos\theta > 0$.

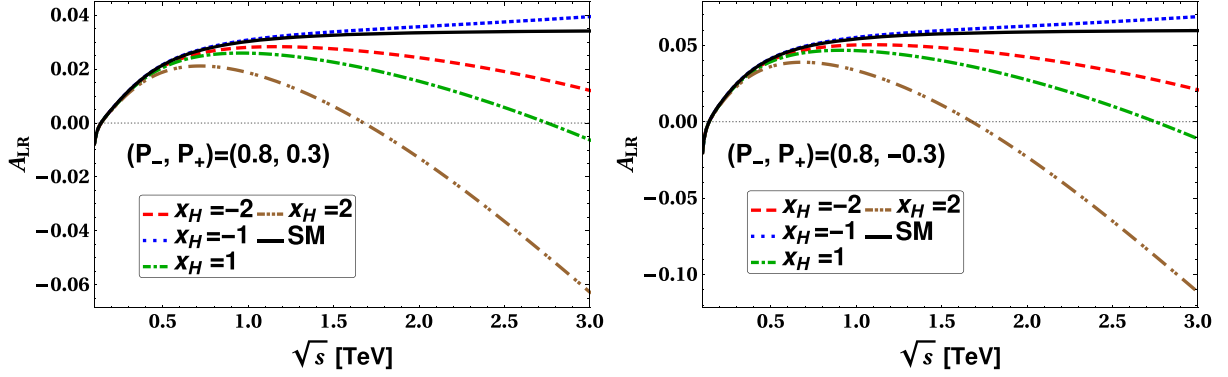


FIG. 21. Integrated LR asymmetry as a function of \sqrt{s} for $x_H = -2, -1, 1$ and 2 considering $M_{Z'}/g' = 7.5$ TeV and $g' = 0.4$. The SM result is represented by the black solid line.

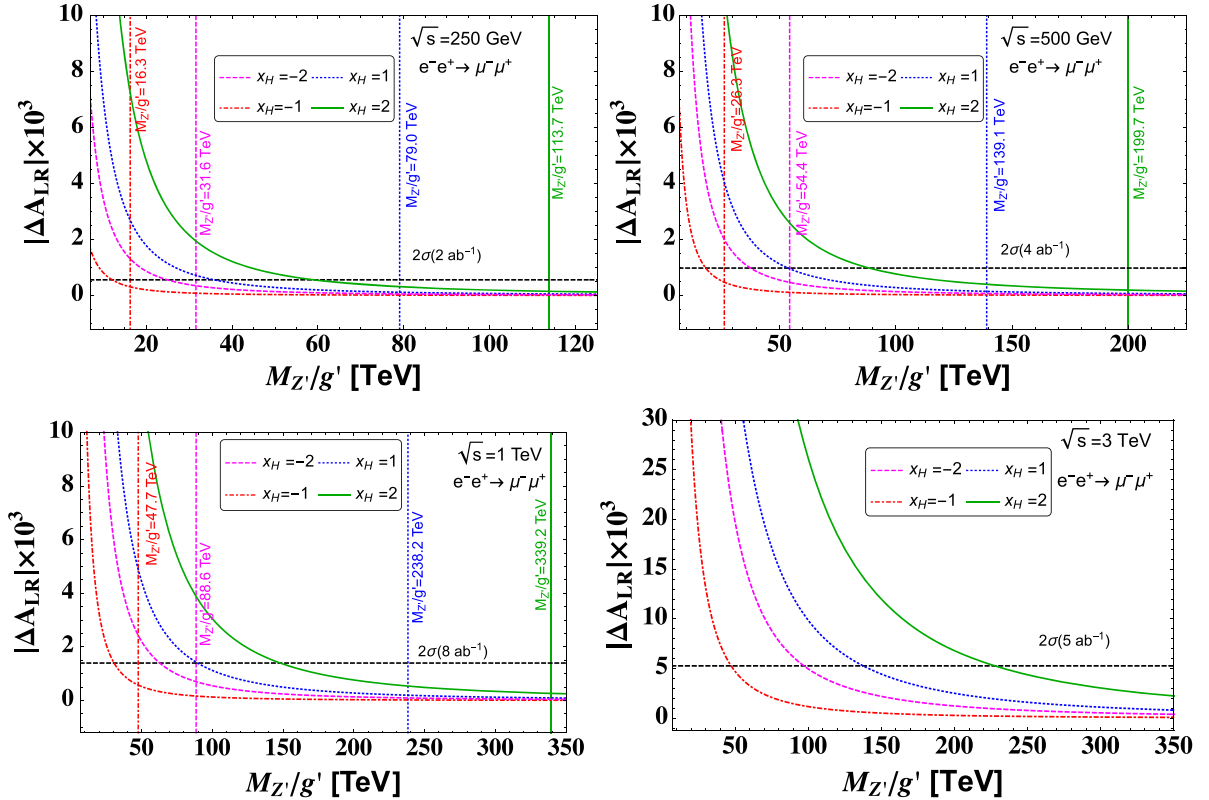


FIG. 22. Integrated LR asymmetry as a function of $M_{Z'}/g'$ for different values of x_H and \sqrt{s} using the $e^- e^+ \rightarrow \mu^- \mu^+$ process. The corresponding upper bounds on $M_{Z'}/g'$ (vertical lines) from Table III and Fig. 2 estimated from Ref. [46] are also shown for comparison.

The integrated LR asymmetry is shown in Fig. 21 for two polarizations $(P_-, P_+) = (0.8, 0.3)$ and $(0.8, -0.3)$ considering $x_H = -2, -1, 1, \text{ and } 2$. We fix $M_{Z'} = 7.5$ TeV. The integrated LR asymmetries for different x_H (except $x_H = -1$) significantly deviate from the SM result with the increase in \sqrt{s} . The $x_H = 2$ case shows the maximum deviation and is of opposite sign to the SM prediction as we go to higher \sqrt{s} .

V. DISCUSSION

The various kinematic observables discussed in this work can be used as a postdiscovery tool to distinguish between different x_H charges in our chiral $U(1)$ scenario where the Z' differently interacts with the left- and right-handed fermions. To illustrate this point, let us take the $e^+e^- \rightarrow \mu^+\mu^-$ process as an example and consider the deviation of the integrated left-right asymmetry $\Delta\mathcal{A}_{\text{LR}}$ from the SM prediction. This is plotted in Fig. 22 as a function of $M_{Z'}/g'$ for different x_H values and for different \sqrt{s} . We find that the deviations can exceed 2σ (shown by the horizontal dashed line) for a wide range of $M_{Z'}/g'$. For comparison, we also show the corresponding 95% C.L. upper bounds on $M_{Z'}/g'$ (vertical lines, cf. Fig. 2 and Table III) derived from the limits on the effective scales from Ref. [46]. We note that while a simple recasting of the contact interaction analysis in Ref. [46] gives a slightly larger reach for $M_{Z'}/g'$ as compared to $\Delta\mathcal{A}_{\text{LR}}$ by itself, the latter can be used as a precision tool to probe x_H once a deviation in the total cross section is seen for a given $M_{Z'}/g'$. The other fermion-pair final states considered in previous sections ($b\bar{b}, t\bar{t}, e^+e^-$) give similar results as in Fig. 22. In principle, all the other kinematic variables discussed here can be combined into a multivariate analysis which could potentially enhance the sensitivity reach in $M_{Z'}/g'$ as well, but this is beyond the scope of the current work.

VI. CONCLUSION

We have shown that the general $U(1)_X$ scenario can be effectively probed via the fermion pair production process at future e^-e^+ colliders, even when the associated Z' boson is well beyond the kinematic reach of the colliders. This will be possible by precisely measuring the deviations of the differential and integrated scattering cross sections, as well as the FB, LR, and LR-FB asymmetries, from their SM-predicted values. In particular, since the asymmetries are the ratios of (differential or integral) cross sections, their deviations from the SM values highly depend on the $U(1)_X$ charges. In fact, we observe significant deviations from the SM for several choices of the charge x_H considering the limits on the $U(1)_X$ gauge coupling depending on $M_{Z'}$. Hence we expect that FB, LR, and LR-FB asymmetries can be successfully probed in e^-e^+ colliders to test and characterize multi-TeV Z' bosons coupling differently to left- and right-handed fermions.

ACKNOWLEDGMENTS

A. D. would like to thank Hisaki Hatanaka, Daniel Jeans, Takaaki Nomura, and Junping Tian for useful information regarding ILC. The work of A. D. was supported by the National Research Foundation of Korea (NRF) grant funded by the Korean government (NRF-2020R1C1C1012452). The work of B. D. is supported in part by the U.S. Department of Energy under Grant No. DE-SC0017987, by the Neutrino Theory Network Program, and by a Fermilab Intensity Frontier Fellowship. The work of Y. H. is supported by the Japan Society for the Promotion of Science, Grants-in-Aid for Scientific Research, No. 19K03873. The work of S. M. is supported by the Spanish Grant No. FPA2017-85216-P (AEI/FEDER, UE) and PROMETEO/2018/165 (Generalitat Valenciana).

-
- [1] P. Zyla *et al.* (Particle Data Group Collaboration), Review of particle physics, *Prog. Theor. Exp. Phys.* **2020**, 083C01 (2020).
 - [2] A. Leike, The phenomenology of extra neutral gauge bosons, *Phys. Rep.* **317**, 143 (1999).
 - [3] P. Langacker, The physics of heavy Z' gauge bosons, *Rev. Mod. Phys.* **81**, 1199 (2009).
 - [4] J. C. Pati and A. Salam, Lepton number as the fourth color, *Phys. Rev. D* **10**, 275 (1974); Erratum, *Phys. Rev. D* **11**, 703 (1975).
 - [5] R. Mohapatra and J. C. Pati, A natural left-right symmetry, *Phys. Rev. D* **11**, 2558 (1975).
 - [6] G. Senjanovic and R. N. Mohapatra, Exact left-right symmetry and spontaneous violation of parity, *Phys. Rev. D* **12**, 1502 (1975).
 - [7] H. Georgi, The state of the Art—Gauge theories, *AIP Conf. Proc.* **23**, 575 (1975).
 - [8] H. Fritzsch and P. Minkowski, Unified interactions of leptons and hadrons, *Ann. Phys. (N.Y.)* **93**, 193 (1975).
 - [9] F. Gursey, P. Ramond, and P. Sikivie, A universal gauge theory model based on E6, *Phys. Lett.* **60B**, 177 (1976).
 - [10] Y. Achiman and B. Stech, Quark lepton symmetry and mass scales in an E6 unified gauge model, *Phys. Lett.* **77B**, 389 (1978).
 - [11] Y. Hosotani, Dynamical mass generation by compact extra dimensions, *Phys. Lett.* **126B**, 309 (1983).
 - [12] K. Agashe, R. Contino, and A. Pomarol, The Minimal composite Higgs model, *Nucl. Phys.* **B719**, 165 (2005).

- [13] A. D. Medina, N. R. Shah, and C. E. Wagner, Gauge-Higgs unification and radiative electroweak symmetry breaking in warped extra dimensions, *Phys. Rev. D* **76**, 095010 (2007).
- [14] Y. Hosotani, K. Oda, T. Ohnuma, and Y. Sakamura, Dynamical electroweak symmetry breaking in $SO(5) \times U(1)$ Gauge-Higgs unification with top and bottom quarks, *Phys. Rev. D* **78**, 096002 (2008); Erratum, *Phys. Rev. D* **79**, 079902 (2009).
- [15] S. Funatsu, H. Hatanaka, Y. Hosotani, Y. Orikasa, and T. Shimotani, Novel universality and Higgs decay $H \rightarrow \gamma\gamma$, gg in the $SO(5) \times U(1)$ gauge-Higgs unification, *Phys. Lett. B* **722**, 94 (2013).
- [16] J. Yoon and M. E. Peskin, Dissection of an $SO(5) \times U(1)$ gauge-Higgs unification model, *Phys. Rev. D* **100**, 015001 (2019).
- [17] S. Schael *et al.* (ALEPH, DELPHI, L3, OPAL, LEP Electroweak Collaborations), Electroweak measurements in electron-positron collisions at W-boson-pair energies at LEP, *Phys. Rep.* **532**, 119 (2013).
- [18] V. M. Abazov *et al.* (D0 Collaboration), Search for a heavy neutral gauge boson in the dielectron channel with 5.4 fb^{-1} of $p\bar{p}$ collisions at $\sqrt{s} = 1.96 \text{ TeV}$, *Phys. Lett. B* **695**, 88 (2011).
- [19] T. Aaltonen *et al.* (CDF Collaboration), Search for High Mass Resonances Decaying to Muon Pairs in $\sqrt{s} = 1.96 \text{ TeV}$ $p\bar{p}$ Collisions, *Phys. Rev. Lett.* **106**, 121801 (2011).
- [20] G. Aad *et al.* (ATLAS Collaboration), Search for high-mass dilepton resonances using 139 fb^{-1} of pp collision data collected at $\sqrt{s} = 13 \text{ TeV}$ with the ATLAS detector, *Phys. Lett. B* **796**, 68 (2019).
- [21] CMS Collaboration, Search for a narrow resonance in high-mass dilepton final states in proton-proton collisions using 140 fb^{-1} of data at $\sqrt{s} = 13 \text{ TeV}$, Report No. CMS-PAS-EXO-19-019.
- [22] Y. Li, F. Petriello, and S. Quackenbush, Reconstructing a Z-prime Lagrangian using the LHC and low-energy data, *Phys. Rev. D* **80**, 055018 (2009).
- [23] T. Appelquist, B. A. Dobrescu, and A. R. Hopper, Nonexotic neutral gauge bosons, *Phys. Rev. D* **68**, 035012 (2003).
- [24] C. Coriano, L. Delle Rose, and C. Marzo, Vacuum stability in $U(1)$ -prime extensions of the Standard Model with TeV scale right handed neutrinos, *Phys. Lett. B* **738**, 13 (2014).
- [25] A. Das, S. Oda, N. Okada, and D.-s. Takahashi, Classically conformal $U(1)'$ extended standard model, electroweak vacuum stability, and LHC Run-2 bounds, *Phys. Rev. D* **93**, 115038 (2016).
- [26] A. Das, S. Goswami, K. Vishnudath, and T. Nomura, Constraining a general $U(1)'$ inverse seesaw model from vacuum stability, dark matter and collider, *Phys. Rev. D* **101**, 055026 (2020).
- [27] A. Davidson, $B - L$ as the fourth color within an $SU(2)_L \times U(1)_R \times U(1)$ model, *Phys. Rev. D* **20**, 776 (1979).
- [28] R. Marshak and R. N. Mohapatra, Quark—lepton symmetry and $B - L$ as the $U(1)$ generator of the electroweak symmetry group, *Phys. Lett.* **91B**, 222 (1980).
- [29] S. Funatsu, H. Hatanaka, Y. Hosotani, Y. Orikasa, and N. Yamatsu, Fermion pair production at e^-e^+ linear collider experiments in GUT inspired gauge-Higgs unification, *Phys. Rev. D* **102**, 015029 (2020).
- [30] G. Altarelli, B. Mele, and M. Ruiz-Altaba, Searching for new heavy vector bosons in $p\bar{p}$ colliders, *Z. Phys. C* **45**, 109 (1989); Erratum, *Z. Phys. C* **47**, 676 (1990).
- [31] P. Minkowski, $\mu \rightarrow e\gamma$ at a rate of one out of 10^9 muon decays?, *Phys. Lett.* **67B**, 421 (1977).
- [32] R. N. Mohapatra and G. Senjanovic, Neutrino Mass and Spontaneous Parity Nonconservation, *Phys. Rev. Lett.* **44**, 912 (1980).
- [33] T. Yanagida, Horizontal gauge symmetry and masses of neutrinos, Conf. Proc. C **7902131**, 95 (1979).
- [34] M. Gell-Mann, P. Ramond, and R. Slansky, Complex spinors and unified theories, Conf. Proc. C **790927**, 315 (1979).
- [35] S. Glashow, The future of elementary particle physics, *NATO Sci. Ser. B* **61**, 687 (1980).
- [36] A. Das, N. Okada, and N. Papapietro, Electroweak vacuum stability in classically conformal $B - L$ extension of the Standard Model, *Eur. Phys. J. C* **77**, 122 (2017).
- [37] A. Das, N. Okada, and D. Raut, Enhanced pair production of heavy Majorana neutrinos at the LHC, *Phys. Rev. D* **97**, 115023 (2018).
- [38] A. Das, N. Okada, and D. Raut, Heavy Majorana neutrino pair productions at the LHC in minimal $U(1)$ extended Standard Model, *Eur. Phys. J. C* **78**, 696 (2018).
- [39] A. Das, N. Okada, S. Okada, and D. Raut, Probing the seesaw mechanism at the 250 GeV ILC, *Phys. Lett. B* **797**, 134849 (2019).
- [40] A. Das, P. S. B. Dev, and N. Okada, Long-lived TeV-scale right-handed neutrino production at the LHC in gauged $U(1)_X$ model, *Phys. Lett. B* **799**, 135052 (2019).
- [41] C.-W. Chiang, G. Cottin, A. Das, and S. Mandal, Displaced heavy neutrinos from Z' decays at the LHC, *J. High Energy Phys.* **12** (2019) 070.
- [42] E. Eichten, K. D. Lane, and M. E. Peskin, New Tests for Quark and Lepton Substructure, *Phys. Rev. Lett.* **50**, 811 (1983).
- [43] LEP, ALEPH, DELPHI, L3, OPAL, LEP Electroweak Working Group, SLD Electroweak Group, SLD Heavy Flavor Group Collaborations, A combination of preliminary electroweak measurements and constraints on the standard model, [arXiv:hep-ex/0312023](https://arxiv.org/abs/hep-ex/0312023).
- [44] H. Kroha, Compositeness limits from $E^+ E^-$ annihilation revisited, *Phys. Rev. D* **46**, 58 (1992).
- [45] M. Carena, A. Daleo, B. A. Dobrescu, and T. M. Tait, Z' gauge bosons at the Tevatron, *Phys. Rev. D* **70**, 093009 (2004).
- [46] K. Fujii *et al.* (LCC Physics Working Group Collaboration), Tests of the standard model at the international linear collider, [arXiv:1908.11299](https://arxiv.org/abs/1908.11299).
- [47] ATLAS Collaboration, Search for new phenomena in Dijet events using 139 fb^{-1} of pp collisions at $\sqrt{s} = 13 \text{ TeV}$ collected with the ATLAS Detector, Report No. ATLAS-CONF-2019-007, 2019.
- [48] A. M. Sirunyan *et al.* (CMS Collaboration), Search for narrow and broad dijet resonances in proton-proton collisions at $\sqrt{s} = 13 \text{ TeV}$ and constraints on dark matter mediators and other new particles, *J. High Energy Phys.* **08** (2018) 130.
- [49] ATLAS Collaboration, Technical Design Report for the Phase-II Upgrade of the ATLAS LAr Calorimeter, Technical

- Reports No. CERN-LHCC-2017-018, No. ATLAS-TDR-027, CERN, Geneva, 2017, <https://cds.cern.ch/record/2285582>.
- [50] A. Das and S. Mandal, FeynRules file for the general U(1) extended SM, <https://feynrules.irmp.ucl.ac.be/wiki/GeneralU1>.
- [51] A. Abada *et al.* (FCC Collaboration), FCC-ee: The Lepton Collider: Future Circular Collider Conceptual Design Report Volume 2, *Eur. Phys. J. Spec. Top.* **228**, 261 (2019).
- [52] CEPC Study Group Collaboration, CEPC conceptual design report: Volume 1—Accelerator, [arXiv:1809.00285](https://arxiv.org/abs/1809.00285).
- [53] T. Barklow, J. Brau, K. Fujii, J. Gao, J. List, N. Walker, and K. Yokoya, ILC operating scenarios, [arXiv:1506.07830](https://arxiv.org/abs/1506.07830).
- [54] T. Charles *et al.* (CLICdp, CLIC Collaborations), The compact linear collider (CLIC)—2018 Summary report, [arXiv:1812.06018](https://arxiv.org/abs/1812.06018).
- [55] P. Bambade *et al.*, The international linear collider: A global project, [arXiv:1903.01629](https://arxiv.org/abs/1903.01629).
- [56] P. Fileviez Perez, C. Murgui, and S. Ohmer, Simple left-right theory: Lepton number violation at the LHC, *Phys. Rev. D* **94**, 051701 (2016).
- [57] B. Schrempp, F. Schrempp, N. Wermes, and D. Zeppenfeld, Bounds on new contact interactions from future e^+e^- colliders, *Nucl. Phys.* **B296**, 1 (1988).
- [58] D. Kennedy, B. Lynn, C. Im, and R. Stuart, Electroweak cross-sections and asymmetries at the Z0, *Nucl. Phys.* **B321**, 83 (1989).
- [59] ALEPH, CDF, D0, DELPHI, L3, OPAL, SLD, LEP Electroweak Working Group, Tevatron Electroweak Working Group, SLD Electroweak, Heavy Flavour Groups Collaborations, Precision electroweak measurements and constraints on the standard model, [arXiv:1012.2367](https://arxiv.org/abs/1012.2367).
- [60] G. Moortgat-Pick *et al.*, The role of polarized positrons and electrons in revealing fundamental interactions at the linear collider, *Phys. Rep.* **460**, 131 (2008).
- [61] M. Baak *et al.*, Working group report: Precision study of electroweak interactions, in *Proceedings of the Community Summer Study 2013: Snowmass on the Mississippi, 2013*, [arXiv:1310.6708](https://arxiv.org/abs/1310.6708).
- [62] S. Schael *et al.* (ALEPH, DELPHI, L3, OPAL, SLD, LEP Electroweak Working Group, SLD Electroweak Group, SLD Heavy Flavour Group Collaborations), Precision electroweak measurements on the Z resonance, *Phys. Rep.* **427**, 257 (2006).
- [63] A. Blondel, B. Lynn, F. Renard, and C. Verzegnassi, Precision measurements of final state weak coupling from polarized electron—positron annihilation, *Nucl. Phys.* **B304**, 438 (1988).
- [64] K. Abe *et al.* (SLD Collaboration), Measurement of A(b) and A(c) from the Left-Right Forward—Backward Asymmetry of Leptons in Hadronic Events at the Z0 Resonance, *Phys. Rev. Lett.* **74**, 2895 (1995).
- [65] K. Abe *et al.* (SLD Collaboration), Measurement of A(b) from the Left-Right Forward—Backward Asymmetry of b Quark Production in Z0 Decays using a Momentum Weighted Track Charge Technique, *Phys. Rev. Lett.* **74**, 2890 (1995).
- [66] K. Abe *et al.* (SLD Collaboration), Measurement of the Left-Right Forward—Backward Asymmetry for Charm Quarks with D^{*+} and D^+ Mesons, *Phys. Rev. Lett.* **75**, 3609 (1995).